CHALMERS
UNIVERSITY OF TECHNOLOGY

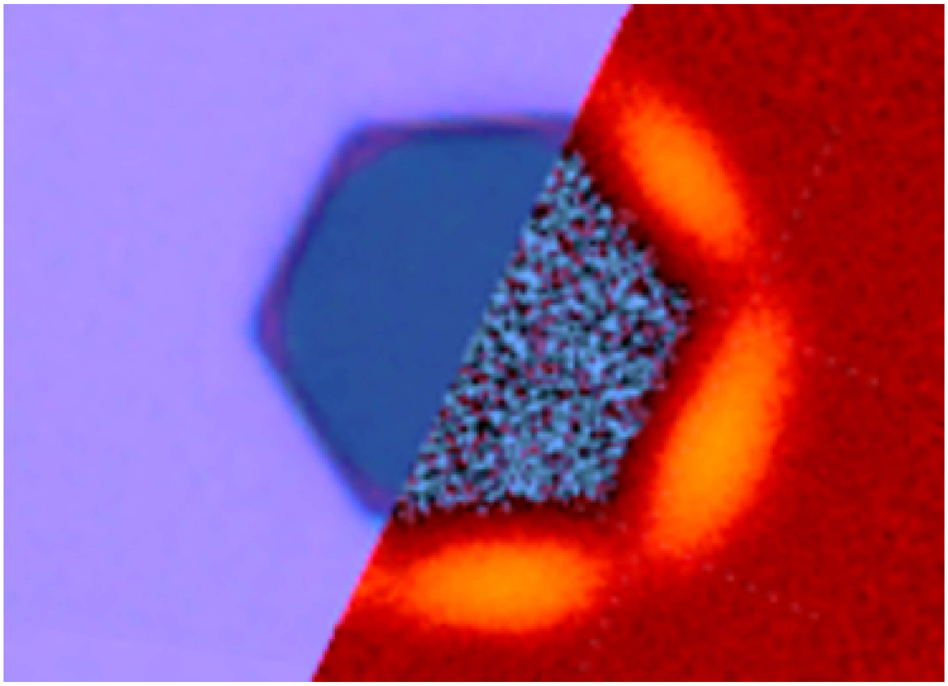

Spectroscopic Characterization of Edges in Transition Metal Dichalcogenide Metastructures

New playgrounds for one-dimensional physics

Master's thesis in Physics

ADRIÁN DEWAMBRECHIES FERNÁNDEZ

DEPARTMENT OF PHYSICS

CHALMERS UNIVERSITY OF TECHNOLOGY
Gothenburg, Sweden 2022
www.chalmers.se

MASTER'S THESIS 2022

Spectroscopic Characterization of Edges in Transition Metal Dichalcogenide Metastructures

New playgrounds for one-dimensional physics

ADRIÁN DEWAMBRECHIES FERNÁNDEZ

Department of Physics
Division of Nano and Biophysics
Shegai Group
CHALMERS UNIVERSITY OF TECHNOLOGY
Gothenburg, Sweden 2022

Spectroscopic Characterization of Edges in Transition Metal Dichalcogenide Metastructures
New playgrounds for one-dimensional physics
ADRIÁN DEWAMBRECHIES FERNÁNDEZ

© ADRIÁN DEWAMBRECHIES FERNÁNDEZ, 2022.

Supervisor: Timur Shegai
Examiner: Timur Shegai

Master's Thesis 2022
Department of Physics
Division of Nano and Biophysics
Shegai Group
Chalmers University of Technology
SE-412 96 Gothenburg
Telephone +46 31 772 1000

Cover: Superposition of optical image and Second Harmonic Generation scan over a hexagonal metastructure in MoS_2.

Typeset in LaTeX
Printed by Chalmers Reproservice
Gothenburg, Sweden 2022

Spectroscopic Characterization of Edges in Transition Metal Dichalcogenide Metastructures
New playgrounds for one-dimensional physics
ADRIÁN DEWAMBRECHIES FERNÁNDEZ
Department of Physics
Chalmers University of Technology

Abstract

Two-dimensional materials have proven to show a very broad spectrum of physical phenomena for the past decades, offering a very important scientific playground, both under an experimental and theoretical point of view. While the family of Transition Metal Dichalcogenides (TMDCs) has overcome most of the problems that prevented graphene to consolidate as a reliable material for a scalable integrated circuit implementation, they still face their own challenges regarding device-to-device variability, and requirements for industry-scalable dimensions.

The next step in the understanding of two-dimensional materials is the study of the physics taking place at the edges, which can be very different from its bulk counterpart, these differences ultimately coming from the symmetry breaking in the crystal structure and its consequences on the electronic properties. In this context, this thesis is focused on the characterization of these one-dimensional defects that can be produced in a new kind of metastructures taking place on different TMDC multilayers, with very high-quality in their crystal symmetry and optoelectronic properties. The project will start with production of these physical systems, followed by their characterization via optical and mechanical means, in particular Raman spectroscopy, Second Harmonic Generation (SHG), Scanning Electron Microscopy (SEM) and Atomic Force Microscopy (AFM).

This complete vision coming from different corners of the characterization will enlighten the growth process of these metastructures, testing their reliability as a system where the understanding of edge physics can be promoted and developed.

Keywords: TMDC, Raman spectroscopy, Second Harmonic Generation, Edge physics.

Acknowledgements

Many people to be thankful to here!

First and foremost, to all my group colleagues at Shegai group. In particular, Timur Shegai, for accepting me in the group in the first place and always keeping the door open for supervision, guidance and interesting discussions, for taking time to come to the lab and investing effort for becoming a better professor. Also to Betül Kücüköz and Aleksandr Poliakov, for all the time they invested into my training in the cleanroom and the lab, an invaluable help that made the completion of this work possible. To Adriana, for her will to always help others, the warm welcome and all the useful advice. To Gosha, Abhay and Oleg for all the discussions and guidance that eventually helped me move forward and learn how to do science. Without the support of these people nothing would have been possible.

Secondly, to all the corridor colleagues in the sixth floor I shared my days with, always keen for giving out a kind smile or sharing some laughs in the lunchroom. You made everyday's work way more fun and pleasant!

Next, to my family back in Spain for the continuous support since the day I announced them I wanted to move to the far north. Their affection held me up to enjoy these two years to the fullest. Also to my family here in Gothenburg: my girlfriend Camille for being the kindest person in this world and willing to share her path with me, for which I love her. To Wassim and Basia for their kindness and for always being there when needed. To my multiple friends, old and new, from all over the world that made the journey worth living, and the decision to come to Sweden one of the best of my life.

And finally, to the city of Gothenburg and Chalmers University for accepting me in their community, and offering me a place to grow both professionally and personally.

For all this and way more, I am grateful.

Adrián Dewambrechies Fernández, Gothenburg, June 2022

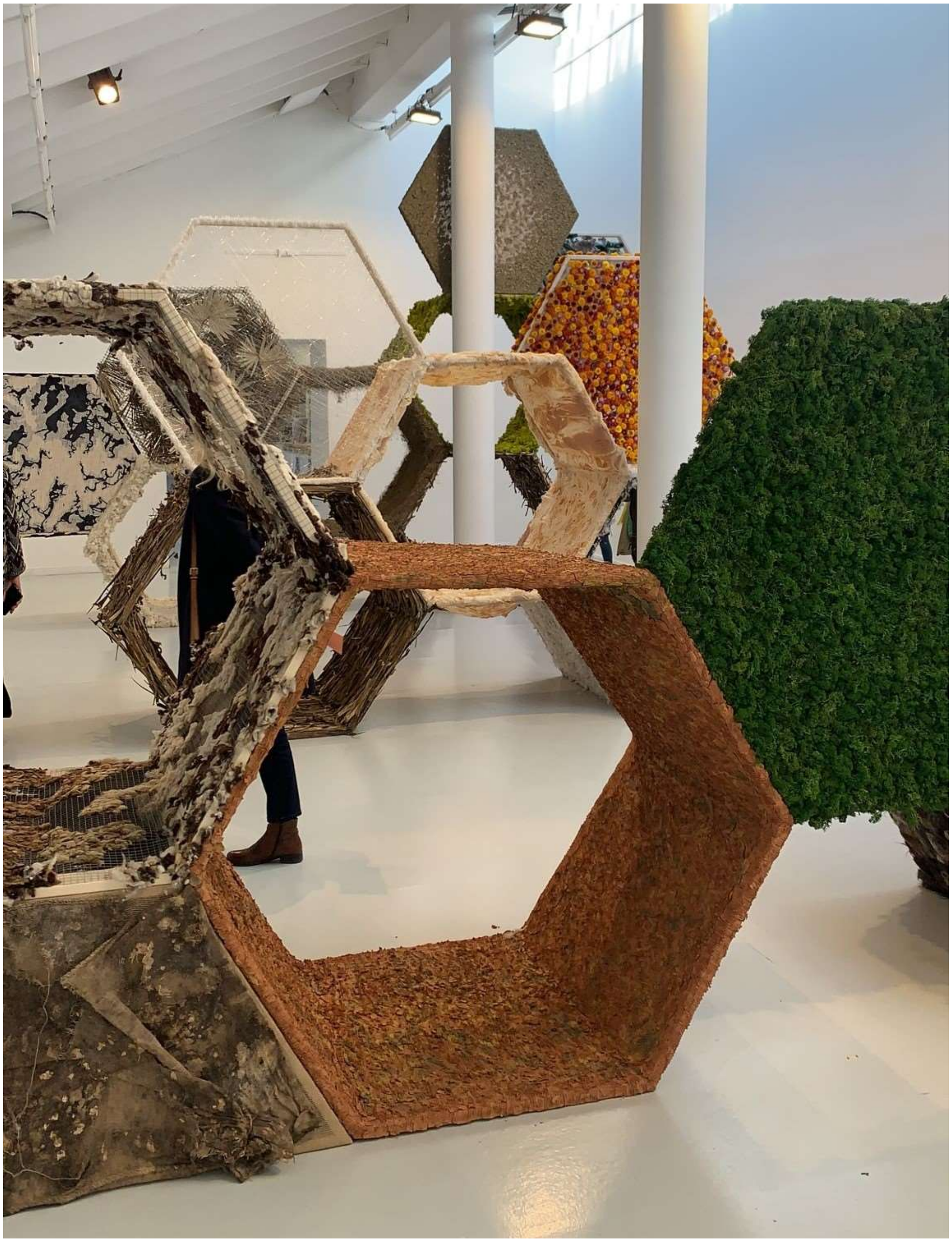

Louisa Raddatz, La Maison des vivants
La Ferme du Buisson, Paris, 2022

Contents

List of Acronyms xii

List of Figures xiv

List of Tables xix

1 Introduction 1

2 Theoretical Framework 5
- 2.1 Transition metal dichalcogenides . . . 5
- 2.2 Raman spectroscopy . . . 8
- 2.3 Second Harmonic Generation . . . 13
- 2.4 TMDC metamaterials with atomic precision . . . 17

3 Methods 19
- 3.1 Sample preparation . . . 19
- 3.2 Metastructure production . . . 20
- 3.3 Raman setup and data analysis . . . 21
- 3.4 SHG setup and data analysis . . . 23
- 3.5 Additional characterization . . . 26

4 Results and Discussion 29
- 4.1 Raman spectroscopy on WS_2 and MoS_2 samples . . . 29
- 4.2 AFM and SEM . . . 32
- 4.3 Raman Spectroscopy on MoS_2 Metastructures . . . 36
- 4.4 Second harmonic generation on MoS_2 metastructures . . . 37

5 Conclusions and Outlook 41

Bibliography 43

A Appendix: SHG intensity derivaiton I

List of Acronyms

Below is the list of acronyms that have been used throughout this thesis listed in alphabetical order:

AFM	Atomic Force Microscopy
CBM	Conduction band minimum
SHG	Second Harmonic Generation
SEM	Scanning Electron Microscopy
TMDC	Transition Metal Dischalcogenide
VBM	Valence band maximum

List of Figures

2.1 Crystallography of the 2H and 1T phases a), d) MoS_2 unit cell showing inversion symmetry b), e) Side view of a MoS_2 bilayer (*a* axis) c), f) Top view of a MoS_2 bilayer (*c* axis) g), h) zigzag and armchair directions respectively, highlighted with dashed lines. 6
2.2 Electronic bandstructure of monolayer and bulk MoS_2, showing the direct bandgap semiconductor and indirect bandgap semimetallic behaviors, respectively. Adapted from [8]. 8
2.3 Visualization of the Raman active vibrational modes for a 2H monolayer of TMDC (left) and the associated frequency shifts for MoS_2 (right) 9
2.4 Visualization of the Raman active vibrational modes for a 2H bilayer/bulk of TMDC (left) and the associated frequencies for bulk MoS_2 (right) 10
2.5 Literature review of Raman spectra under an external perturbation, for MoS_2 and WS_2. We show the peak position dependance with a) d) number of layers, N b) e) tensile strain, ϵ c) f) temperature, T. Adapted from references [24], [18][3]. 12
2.6 Polarization dependance for the normalized SHG signal intensity coming from an MoS_2 monolayer, showing higher intensity along the zigzag directions of the structure. It follows equation 2.21. 16
2.7 Scheme of the nanopatterning process taking place on the TMDC multilayer i) 2H-TMDC sample lying on SiO_2/Si substrate ii) flake is dry-etched via electron beam lithography into circular holes iii) wet etching turns circles into hexagonal metastructures ready to be studied. Adapted from [16]. 17
2.8 Optical images of produced metastructures on a) WS_2 (scalebar 5 um) and b) MoS_2 (scalebar 1 um) samples. It is observed a different optical contrast on alternating edges in the MoS_2 sample. The images were taken with a 100x/0.9 objective. 18

3.1 Types of produced metastructures with different diameters and flake thicknesses on a) WS_2 and b) MoS_2. We observe sharper edges on WS_2 samples and distorted hexagonal shapes on MoS_2. Scalebars 10 um. 21
3.2 Silicon peak fitting example. 23

3.3 SHG setup. The fundamental beam (1040 nm) is depicted in red, while the SHG signal (532 nm) is shown in green. The dashed box shows the elements that can be removed from the setup to make unpolarised measurements. 25

3.4 SHG signal verification. a) Gaussian fitting to the signal spectra, centered at 520 nm with double the frequency of the original 1040 nm excitation. b) Integrated power dependance of the fundamental power, showing a quadratic dependance in the logarithmic scale as expected. 25

3.5 Lennard Jones potential, showing the attractive and repulsive zones at both sides of the equilibrium position for the tip-sample distance. . 27

4.1 Raman spectra for bulk MoS_2 and WS_2. PDMS spectra shows no interference of the modes with the TMDC results. 29

4.2 Optical image (left, scale bar 10 um) of a strained region on a few-layer WS_2 due to the exfoliation process, and Raman peak position map (right) showing the peak position of the in-plane mode E_{2g} the different positions on the red box on the optical image. 30

4.3 a) Optical image (scale bar 10 um) of a WS_2 multilayer region with several steps of different heights b) Raman peak position map showing the peak position of the in-plane mode E_{2g} over the different positions on the red box on the optical image c) Raman spectra on two sites with different thickness on a MoS_2 sample seen on the inset (lateral size of image 10 um) d) Fittings for the peaks in c) 31

4.4 Line scan across flake edge a) optical image of the scanned edge, with the red arrow denoting the scanning direction from inside the flake towards the outside (scale bar 5 um) b) d) fitting of the Raman peaks for both in-plane and out-of-plane modes, respectively c) spectra taken at all the points along the scan. 32

4.5 SEM images. a) Collective vision of all the structures (scalebar 5um) b) 2um hexagon at 1 kV acceleration voltage, showing the topmost layers c) 2 um hexagon at 5 kV acceleration voltage, showing the layers beneath the topmost layers d) enlarged vision of c) at the top-left edge e) tilted vision of the 2 um structure, clearly showing the depleted regions at the three alternating edges due to the absence of material beneath it. 34

4.6 AFM images. a) b) AFM scans of the 2 um structure, whowing contrast for the differently etched edges (scalebars 2 um) c) amplitude section for the red line in a) d) amplitude section for the red line in b). 36

4.7 Raman spectroscopy around MoS_2 hexagonal metastructure a) Optical image of the etched structure with a 2 um diameter (scalebar 1 um) b) Raman scan around the metastructure, showing lower frequencies with lighter colors c) FHWM map of the area d) Raman spectrum performed at the red square, far from the structure. e) Raman spectrum performed at the green square, exactly at the red-shifted area. Peaks are labeled with their shift position. 37

4.8 SHG scans around MoS_2 hexagonal metastructures with different diameters (left) and zoomed around the 2 um diameter structure studied with Raman Spectroscopy. Both panels are shown in log scale for better interpretation of the results. We observe a clear signal increment at the edges, especially at the ones that showed a raman redshift. 38
4.9 Etching process in MoS_2 samples. On the left we have the current situation of the studied metastructure, and on the right we have the proposed structure for a long enough time, when the etching process has removed all the material to make two adjacent triangles. Dashed lines show the shape of the triangle beneath the top layer. . . 40

List of Tables

2.1 Point groups for the different crystal structures seen in a 2H arrangement. 6

3.1 Experimental parameters for the growth of the metastructures to be studied in the experiments. 20

4.1 Experimental results for the in plane (E_{2g}) and out-of-plane (A_{1g}) modes in bulk TMDC samples on PDMS. 29
4.2 $\chi^{(2)}$ components values for the fittings at the polarised measurements shown in Fig. 4.8. 39

1

Introduction

Background

The family of two-dimensional materials has been under the eye of the scientific community for more than two decades now, a journey that started with the successful isolation of graphene back in 2004 [17]. Since then, other 2D materials like phosphorene, hexagonal boron nitride (hBN), 2D oxides or transition metal dichalcogenides (TMDCs) to name a few, have stepped up as candidates to overcome the problems graphene had to consolidate as a reliable material for a scalable integrated circuit implementation.
The promising family of TMDCs attracts significant attention, ever since the reported indirect-direct bandgap transition taking place when isolating a single layer of MoS_2 in 2010 [13], since it was the first demonstration that the distinctive electronic properties of atomically thin materials are not restricted to graphene, but extend to a broader group of Van der Waals bonded solids.
Transistors based on 2D materials are in an accelerating phase towards their implementation in a large-scale integration in integrated circuit technologies. However, there are still big challenges regarding their device-to-device variability and requirements for industry-scalable dimensions, like their contact resistance, doping, mobility or scale length [4]. It is also possible to tune electronic properties via mechanical strain, which has led in the past decade to the birth of an emerging field known as straintronics. The initial motivation for this work was the observation that a WS_2 multilayer behave like rubber under the application of highly localized strain, applied by a tungsten (scan QR code to watch a movie of the experiment), and triggered the interest on what would happen to vibrational and optical properties of the TMDC around these kind of defects. Of special interest is as well the physics taking place at the edges of TMDCs which are susceptible to small changes in the electronic structure like edge states appearing in the semiconducting bandgap [12] [10]. Furthermore, edges are potentially useful for challenging and important applications like hydrogen evolution reaction [9] or gas sensing [11].

The crystal structure of TMDCs allows the existence of two types of edges, similarly to graphene: zigzag and armchair. Each of them may show substantially different properties regarding their electronic struture, magnetism, optics, chemical reactivity, etc. [5][22]. This stresses the importance that one-dimensional defects may have in boosting the understanding of TMDCs and broaden the spectrum of physical phenomena available for interesting applications in the future. The outstanding mechanical properties of TMDCs provide a powerful knob for studying both novel quantum states and developing new device functionalities based on strain and edge

engineering [15], and for
all this, understanding the physics on TMDC sample edges is of particular importance.

https://vimeo.com/713039621

The focus of this MSc Thesis is on the spectroscopic characterization of TMDCs, in particular the strain and edges present on them. Special importance is given to a recently discovered type of hexagonal metastructures produced on multilayer flakes, with reported high-quality edges tunable with atomic precision [16]. Spectroscopic experimental techniques provide a non-invasive acquisition of data on the properties that exhibit some type of light-matter interaction, with the energy of the electromagnetic radiation as the main degree of freedom. Upon this stage, the main questions that drive this thesis are, on the one hand, if there is a correlation between the physics present on the material and its spectroscopic response, and what are the most appropriate experimental techniques to extract and analyse such correlation. Raman Spectroscopy and Second Harmonic Generation (SHG) Spectroscopy allow to obtain information on the phonon vibrations in the material, its symmetry, and quality among others, and have been established as reference techniques for the analysis of these materials. Previous extensive research done on different 2D materials during the last decades has also provided us with solid procedures and standards.

The scope of this work is set by the use of Raman and SHG spectroscopies on metastructures produced on MoS_2 multilayers, complemented by other characterization techniques like scanning electron microscopy (SEM) and atomic force microscopy (AFM). The objectives are to learn the appropriate experimental techniques to prepare the samples and extract data from them, review relevant literature to identify physical concepts and processes taking place in the material during the interaction with light, and finally analyse the extracted data to draw conclusions on how these metastructures can be characterised, in particular close to edges or other defects.

Thesis Outline

This thesis is divided in three main blocks of work. The first one involves a literature review of the most recent publications on TMDCs, their electronic, mechanical and optical properties, as well as a more edge and strain-focused review. This will set the stage for a better understanding of both the context of the problem faced during the project, as well as the physical phenomena that we will encounter. Secondly, there is a nanofabrication process that will involve all the different steps needed to create the aforementioned metastructures on TMDC multilayers. This includes sample exfoliation, transfer onto a suitable substrate, and etching of the metastructures in a cleanroom environment. Finally, the characteriaztion of our TMDC samples will take place on two chapters: a previous study of the physical phenomena taking place on the multilayers (without the metastructures grown on them), shown in previous publications, to check the validity of our experimental setups; followed by the characterization of the hexagons etched on the multilayers, to further understand the physics taking place around them, and their etching process. This characterization will be carried out by spectroscopic (Raman, Second Harmonic Generation, Scanning Electron Microscopy) as well as mechanical (Atomic Force Microcopy) techniques.

2

Theoretical Framework

2.1 Transition metal dichalcogenides

This section offers an overview of the most important theoretical concepts relevant to the thesis development, and the subsequent results. We first show the main properties of the TMDC family concerning its crystal structure and electronic properties, followed by the theory behind the techniques used to characterize our samples. We finally introduce the metastructures that will be the main focus of our studies.

Crystal Structure

TMDCs are Van der Waals-bonded crystals resulting in layered structures, where each unit (MX_2) has a transition metal atom sandwiched between two chalcogens, that will bond together in a hexagonal structure forming different monolayers that are connected via Van der Waals forces. This results in different possible crystalographic structures: trigonal prismatic (2H) and octahedral (1T), see Fig. 2.1. In some cases we can find the 1T distorted version (1T').

- **Trigonal prismatic (2H):** each transition metal is bonded with 6 other nearby chalcogen atoms, three on each side, forming two tetrahedrons that can be seen as a 3-point star from above. The periodicity over the entire layer will thus be seen as hexagonal. This corresponds to an ABA stacking pattern, with both chalcogens occupying the same positions within the planes at both sides of the metal.
  Bulk arrangements have two layers per unit cell (i.e. the structure repeats itself after two layers), thus if we were able to isolate a single monolayer, spatial inversion symmetry would be broken. This will be of great importance in the observed phenomena to be described in the next section.
- **Octahedral (1T):** the only, but as well significant difference with respect to the 2H phase, is a relative rotation of the two tetrahedrons above & below the transition metal of 180°. This will thus be seen from above as two overlapped hexagonal lattices, rotated by 30° with respect to each other. The stacking will now follow an ABC sequence, in contrast with the 2H phase.
- **Distorted octahedral (1T'):** it may happen that the metallic atoms dimerize in pairs, resulting in an attractive force bringing them closer together. In that case, the chalcogens may move upwards/ downwards depending on their position, resulting in an relative displacement in the z axis, δ, and a zigzagged pattern of the trilayer height.

The weak Van der Waals forces that bond the layers together allow to isolate a single monolayer of TMDC. The physical properties and phenomena arisen upon reduction of the number of layers in a bulk TMD form a rich spectrum, as will be shown in the next sections. In fact, bulk TMDCs have been studied for many years now, but the outbreak of 2D materials since the succesful isolation of graphene in 2004 has reactivated the interest in the 2D version of TMDCs.

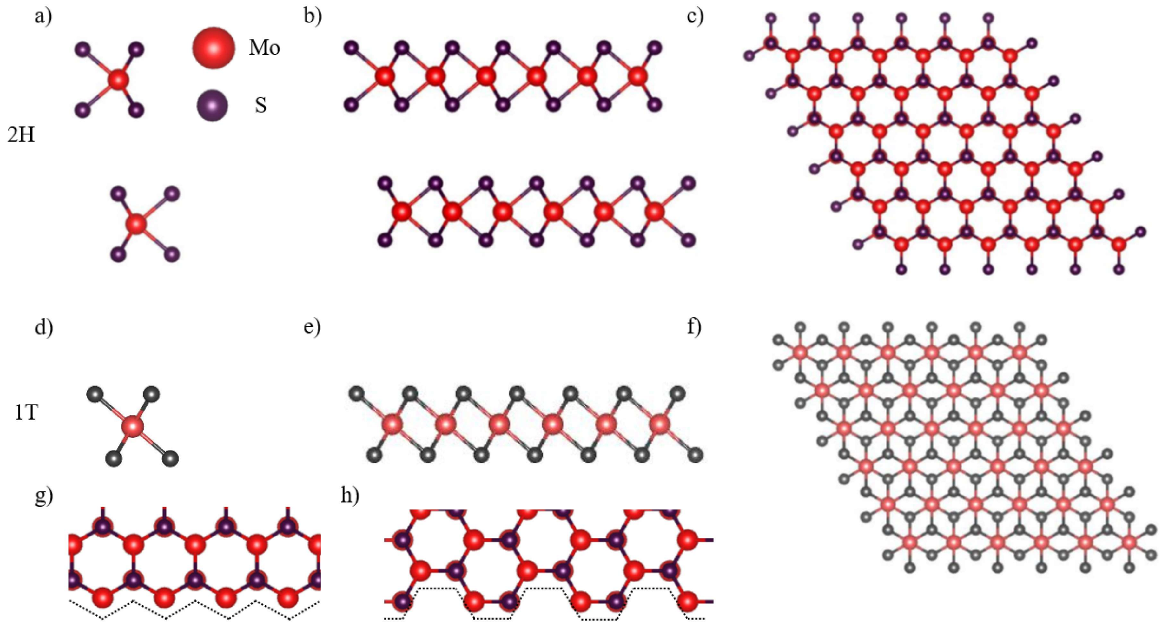

Figure 2.1: Crystallography of the 2H and 1T phases a), d) MoS_2 unit cell showing inversion symmetry b), e) Side view of a MoS_2 bilayer (*a* axis) c), f) Top view of a MoS_2 bilayer (*c* axis) g), h) zigzag and armchair directions respectively, highlighted with dashed lines.

Structure	Point group	Inversion Symmetry
Bulk	C_{6h} ($P6_3/mmc$)	Yes
2 layer	D^3_{3d} ($P\bar{3}m1$)	Yes
1 layer	D^1_{3h} ($P\bar{6}m2$)	No

Table 2.1: Point groups for the different crystal structures seen in a 2H arrangement.

Electronic Properties

Bulk 2H-TMDCs are semimetallic, and by thinning down a sample to a monolayer we recover a semiconducting phase with a 1.9 eV bandgap, see Fig. 2.2. This is the most attractive property of TMDCs, and that triggered the extensive research that takes place nowadays [13]. A hexagonal first Brillouin Zone (BZ) arises from the hexagonal crystallographic arrangement in the monolayer. This BZ shows high-symmetry points at its corners (K points), and are divided into two non-equivalent sets related to each other via time-reversal symmetry (K, K').

From Fig. 2.1 we know the lattice structure for 2H-TMDCs is hexagonal in the top layer. The trigonal prismatic arrangement from the bulk is preserved when turned into a monolayer, but a loss of inversion symmetry takes place. This fact is of key importance for the arisen phenomena that give shape to the monolayer 2H-bandstructure and optoelectronic properties. We will now summarize the key elements that give shape to a monolayer 2H phase:

1. The **first BZ of our monolayer 2H-TMD is hexagonal**, and has two inequivalent sets of high-symmetry points located at its corners (K,K'). We can relate both sets by time reversal symmetry, and they arise from the independent contributions of the two triangular sublattices into which we can divide the real space hexagonal lattice. These two contributions appear as a new degree of freedom for the electrons, the *lattice pseudospin*.
2. **The two sets of K points** can be labelled by yet another degree of freedom, the *valley pseudospin*, because the CBM and VBM are expected to appear exactly at the corners of the BZ. If the band extrema didn't lie at the time-reversal related K points, the valley pseudospin wouldn't be of much interest.
3. **The available orbitals** comming from the transition metal and the chalcogens hybridize in such a way that the electrons behave as *massive Dirac fermions*, and thus they have an effective mass that shapes the CBM and VBM into parabolas with a bandgap between them, and the Fermi level within.
4. **The high Spin-Orbit Coupling (SOC)** in monolayer TMDs, together with the lack of inversion symmetry, produces an important VBM degeneracy breaking. The splitting is reversed for opposite values of the valley pseudospin.

To sum up, monolayer 2H-TMDs behave as direct bandgap semiconductors. They show a key difference with their 3D counterpart, which has an indirect bandgap, semimetallic behavior. An indirect-direct transition is observed upon reduction of the number of layers [13].

Edges in TMDCs

Of particular importance for this thesis is the 2H phase, which is the most stable and found in natural MoS_2 crystals [7]. We now introduce the different types of edges we can find on these samples, as they show a broad spectrum of different physical phenomena and are relevant for the subsequent studies performed in this thesis.

The 2H phase shows a hexagonal crystal structure, and belongs to the C_6 ($P6_3/mmc$) point group. It shows a six-fold rotation symmetry along two different types of inequivalent edges arising from its hexagonal structure, similarly to graphene. Physical properties at edges will change due to the edge and quantum confinement effects, but more precisely, these two different edge terminations showing the highest symmetry are **zigzag and armchair** (see Fig. 2.1 g), h)), and allow the tailoring of their electronic properties, chemical reactivity, optoelectronic properties, etc. [22].

It is strongly supported that zigzag edges in MoS_2 are metallic and magnetic, while zigzag are nonmagnetic semiconductors. They also accept the incorporation of adatoms that may further enrich the spectrum of physical phenomena, altering their stability [5] [22].

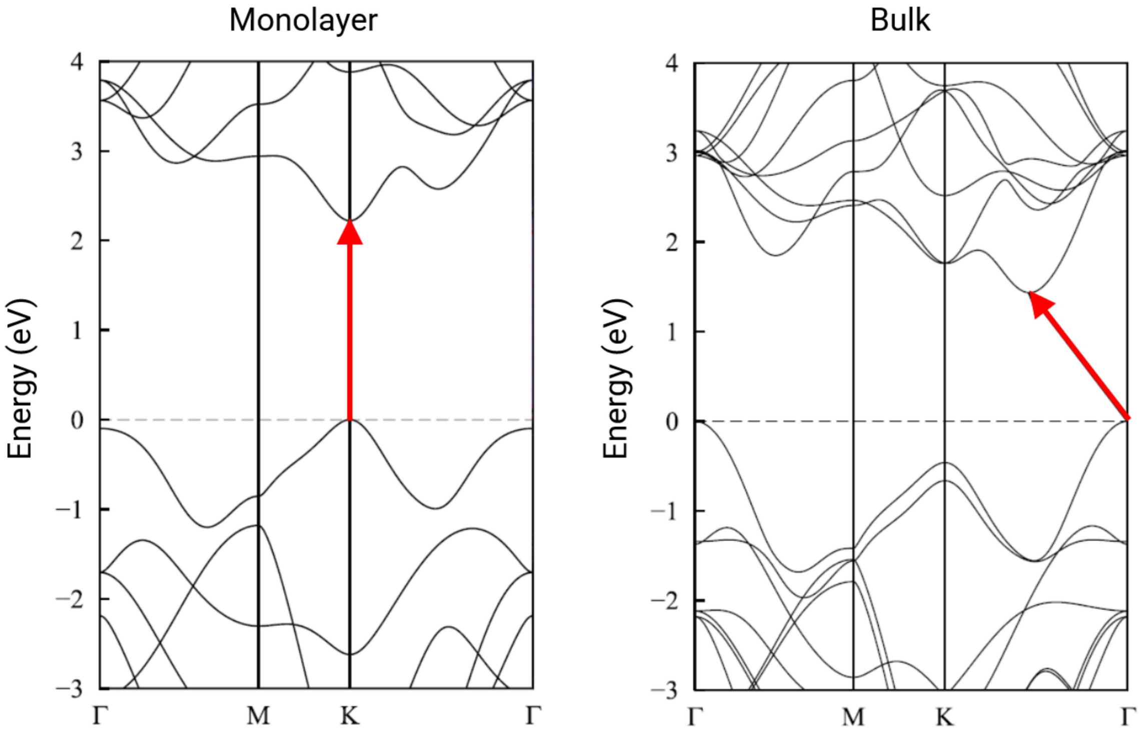

Figure 2.2: Electronic bandstructure of monolayer and bulk MoS_2, showing the direct bandgap semiconductor and indirect bandgap semimetallic behaviors, respectively. Adapted from [8].

2.2 Raman spectroscopy

We will now introduce the theory of Raman scattering, first for a simple molecule to then generalize for a crystal, in particular TMDCs. A crystalline piece of material has collective oscillations of its atoms, that vibrate with some frequency, ω_i. These frequencies are not allowed to take any possible value, since a quantum-mechanical treatment of the system can show that it can be seen as a collection of quantum harmonic oscillators with discrete energy levels. Thus, these collective oscillations of the material have discrete allowed values for their frequency, and the particle associated to these discrete frequencies are called **phonons**.

Raman spectroscopy is a technique that relies on the interaction of an incoming electromagnetic wave (i.e. light) with the optical phonons (i.e. can couple to light) in the material, whose frequency ω_i will depend on the crystal structure and composition.

Vibrational modes in TMDCs

We will go through all the allowed vibrational modes in a 2H TMDC crystal structure. When we go through the Raman theory, we will see that only some of these vibrations are detectable by this technique, thus we will highlight the Raman active modes in red text below. Modes are shown for a monolayer and multilayer separately.

Monolayer

We saw in Table 2.1 that a monolayer (1L) belongs to the point group D^1_{3h}, which has an irreducible representation of the form $\Gamma_{1L} = 2A_2'' + A_1' + 2E' + E''$ [24]. The Raman active modes (i.e. the ones with non-zero Raman tensor elements around equilibrium) are shown in Fig. 2.3, for example in A'_1 we see the chalcogen atoms vibrate out-of phase with respect to each other in the out-of-plane direction.

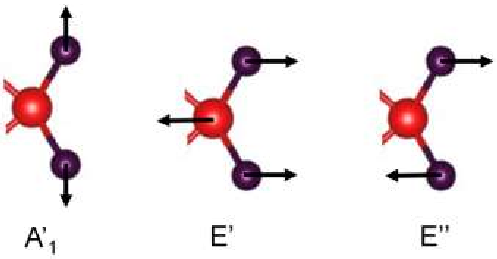

Mode	Raman Shift (cm^{-1})
A'_1	403
E'	384
E''	297

Figure 2.3: Visualization of the Raman active vibrational modes for a 2H monolayer of TMDC (left) and the associated frequency shifts for MoS_2 (right)

Bulk and bilayer

The two crystal structures show inversion symmetry and have irreducible representations $\Gamma_{2L} = 3(A_{1g} + A_{2u} + E_g + E_u)$ and $\Gamma_{bulk} = A_{1g} + 2A_{2u} + 2B_{2g} + B_{1u} + E_{1g} + 2E_{1u} + 2E_{2g} + E_{2u}$. The latter is especially interesting for us since we will be working with multilayers that can be considered bulk. We observe an out-of plane mode A_{1g} and a doubly-degenerate in-plane mode E_{2g}. Notice that these vibrations take place between atoms within the same layer, but we could also have modes where all the atoms are still and the two layers vibrate out of phase perpendicular to the plane, called layer-breathing modes (LBM) or parallel to the plane, called shearing modes (CM). However, the bonds taking place between atoms within a layer are much stronger than the Van der Waals forces acting between layers, and thus the frequencies of the LBM and CM modes are significantly lower than the modes in Fig. 2.4, which will make them invisible with the available setup, since the spectral width of the available laser is so wide that it will 'hide' such low frequency modes.

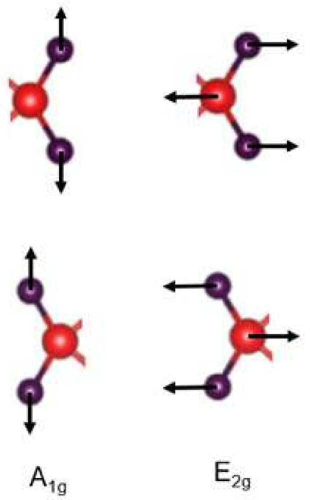

Mode	Raman Shift (cm^{-1})
A_{1g}	408
E^1_{2g}	382

Figure 2.4: Visualization of the Raman active vibrational modes for a 2H bilayer/bulk of TMDC (left) and the associated frequencies for bulk MoS_2 (right)

Raman scattering for a molecule

As a first approach to the problem[1], we try to calculate the induced dipole moment on a single molecule by an incoming, linearly polarised field $\vec{E}$ of frequency ω_1 [2]. The resulting dipole moment will be proportional to the incoming field through the polarizability tensor $\overline{\alpha}$:

$$\vec{p} = \overline{\alpha}\vec{E} \tag{2.1}$$

The polarizability is a function of the positions of the atoms in the molecule, and we will allow them to vibrate around their equilibrium position with a small amplitude. To check the change of the polarizability components with respect to these vibrations we can Taylor expand them, with respect to the normal coordinates of the vibrations:

$$\alpha_{ij} = (\alpha_{ij})_0 + \sum_k \left(\frac{\partial \alpha_{ij}}{\partial Q_k}\right)_0 Q_k + \frac{1}{2}\sum_{k,l}\left(\frac{\partial^2 \alpha_{ij}}{\partial Q_k Q_l}\right)_0 Q_k Q_l + ... \tag{2.2}$$

Here, $Q_k, Q_l, ...$ are the coordinates associated with avery possible molecule vibration present in the structure $\omega_k, \omega_l, ...$ but for our purposes we can only consider one of them (i.e. vibration along one direction only) to qualitatively understand Raman scattering. We thus find an expression for the polarizability up to first order for a single vibration of frequency ω_k:

$$\begin{aligned} \alpha_{ij} &= (\alpha_{ij})_0 + (\alpha'_{ij})Q_k \\ (\alpha'_{ij}) &= \left(\frac{\partial \alpha_{ij}}{\partial Q_k}\right)_0 \qquad \textit{(Raman tensor)} \end{aligned} \tag{2.3}$$

---

[1] For our purposes, the treatment of the vibrations and the EM field will be entire classical. A quantum approach is useful to address more complex details of Raman scattering. Furthermore, we assume that the field's frequency is far enough from any vibrational, rotational or electronic frequency, i.e. we are in a non-resonant condition.

And since we considered only first order atomic vibrations, we have a harmonic motion of the normal coordinates $Q_k = Q_0 cos(\omega_k t + \delta_k)$. We are now in position of finding an expression for the dipole moment produced by the molecule given a linearly polarised incoming field of frequency ω_1:

$$\begin{gathered} \vec{E} = \vec{E_0} cos(\omega_1 t) \\ \vec{p} = \overline{\alpha}_0 \vec{E_0} cos(\omega_1 t) + \overline{\alpha}' Q_0 \vec{E_0} cos(\omega_k t + \delta_k) cos(\omega_1 t) \end{gathered} \tag{2.4}$$

And by using the identity $cosAcosB = [cos(A+B) + cos(A-B)]/2$ and grouping elements dependent in the same frequency, we get an expression for $\vec{p}$ dependent on ω_1, $\omega_1 + \omega_k$ and $\omega_1 - \omega_k$:

$$\vec{p} = \vec{p}(\omega_1) + \vec{p}(\omega_1 + \omega_k) + \vec{p}(\omega_1 - \omega_k) \tag{2.5}$$

Which is already telling us that the induced dipole on the molecule, which will itself produce new radiation that can be collected and analysed, shows two components with shifted frequencies $\omega_1 - \omega_k$ (Stokes radiation) and $\omega_1 + \omega_k$ (anti-Stokes radiation). These are the components that will produce the peaks observed in our experiments. Another important detail is that, for a molecule to show Raman scattering (i.e. be **Raman active**), it needs to have non-zero components in the Raman tensor $\overline{\alpha}'$, i.e. the polarizability as a function of the normal coordinate needs to have non-zero slope at the equilibrium position. We mentioned that the polarizability tensor is dependent on the atoms' positions, thus if they are symmetric with respect to the equilibrium distribution as we oscillate around the normal coordinate, then the mode will not be Raman active. If the distribution of the positions is asymmetric in the two sides of the oscillation, then we will receive Raman signal.

Raman scattering for a solid crystal

In a broader perspective, Raman scattering is an inelastic process that involves the annihilation of an incoming photon ω_L and the creation of an outgoing photon ω_s. The frequency difference between these two will depend on the inelastic interaction of the incoming photon with some elementary excitation in the system, i.e. not only phonons. In the case of crystals, Raman scattering can obtain information from phonons, magnons, impurity vibrational modes and elementary excitations of bulk and low-dimensional systems [21]. All these excitations are allowed to contribute to the final dipole produced on the scattering medium (now a crystal), but in this thesis we are only interested in the phonon contribution to it. In a reflection geometry (see Sec. 2.2), the intensity of the scattered signal can be found as:

$$I(\omega_L, \omega_s) \propto |\hat{e}_s \overline{\alpha}' \hat{e}_L|^2 \tag{2.6}$$

Where the unit vectors point the polarization direction of the incoming and outgoing fields.

The Raman tensors $\overline{\alpha}'$ for all crystal classes were found long ago with their symmetries. Raman tensors for vibrational modes are symmetric ($\overline{\alpha}'_{ij}$ = $\overline{\alpha}'_{ji}$) except near resonances, where they can be anti-symmetric [20]. In bulk 2H-TMDCs, we find the following Raman tensors for the active modes A_{1g} and E_{2g} [6]:

$$\overline{\alpha}'(A_{1g}) = \begin{pmatrix} a & 0 & 0 \\ 0 & a & 0 \\ 0 & 0 & b \end{pmatrix}; \qquad \overline{\alpha}'(E_{2g}) = \begin{pmatrix} d & d & 0 \\ d & -d & 0 \\ 0 & 0 & 0 \end{pmatrix} \tag{2.7}$$

Raman scattering in MoS_2 and WS_2

We will now go over the main relevant results in the literature regarding Raman spectroscopy on WS_2 and MoS_2 multilayers. These are relevant to choose the appropriate experimental parameters, and for the understanding of future results.
Raman peak position is highly dependent on the number of layers, we observe a general tendency in different TMDCs for the in-plane mode E_{2g} to blueshift (i.e. move to the right) and for the out-of-plane mode to redshift (i.e. move to the left) as the thickness of the sample decreases. Both modes 'squeeze in' compared to the bulk, see Fig. 2.5a), d). There is also a tendency to redshift with an increasing tensile strain, a behavior that is more pronounced for the in-plane mode when the strain is directed in-plane. Furthermore, since this mode is degenerate as we can have vibrations in either direction of the 2D plane (see the 2 in the irreducible representations above), we will observe a degeneracy breaking when a uniaxial in-plane strain is applied, since we break the symmetry of both vibration directions (see Fig. 2.5 b), where the E_{2g} mode splits into two different peaks with increasing strain). Finally, both modes will also experience a linear redshift with increasing temperature, see Fig. 2.5 c), f).

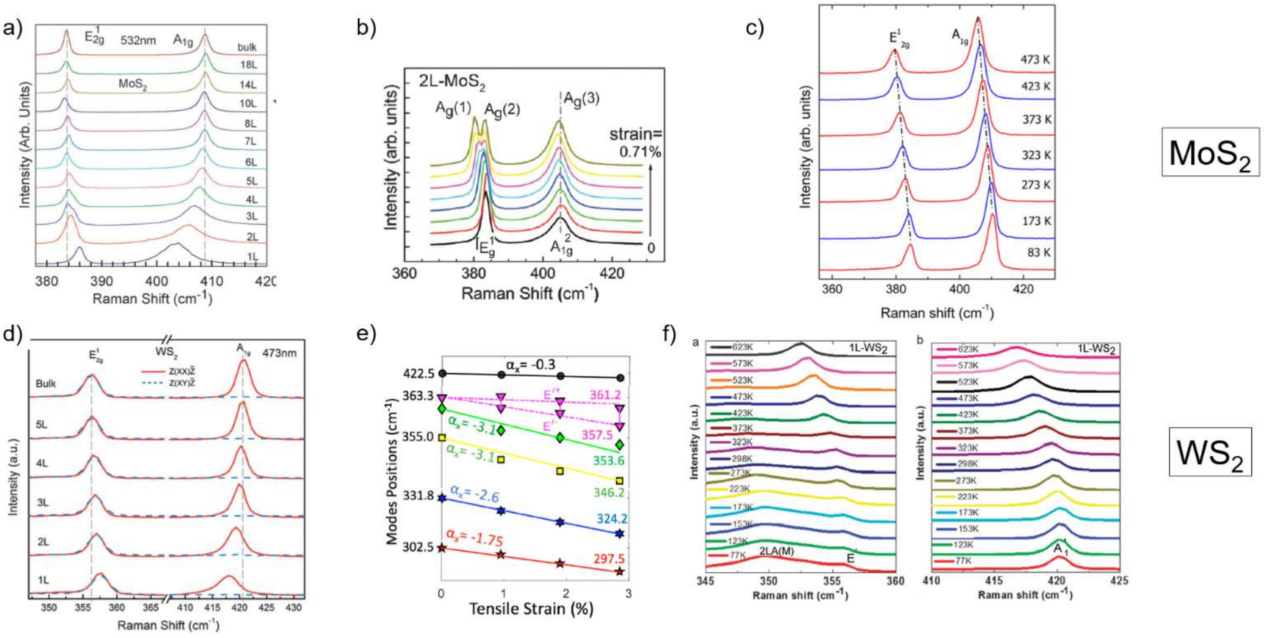

Figure 2.5: Literature review of Raman spectra under an external perturbation, for MoS_2 and WS_2. We show the peak position dependance with a) d) number of layers, N b) e) tensile strain, ϵ c) f) temperature, T. Adapted from references [24], [18][3].

2.3 Second Harmonic Generation

When a piece of material is shone upon with an electromagnetic wave, its response can take shape as an induced polarization $\vec{P}$, which is an average of the dipole moments in a volume of material induced by the incoming light. It has a dominant linear term in the electric field $\vec{E}$, but for high enough fields it can show higher order components:

$$\vec{P}(t) = \epsilon_0[\ \chi^{(1)}E\vec{(t)}\ +\ \chi^{(2)}\vec{E}^2(t)\ +\ \chi^{(3)}\vec{E}^3(t)\ + ...\ ] \tag{2.8}$$

Here we assume that the response is local both in space and time (i.e. the polarization at time t and place $\vec{r}$ does not depend on the polarization at any other previous moment t' or any other place $\vec{r}\,'$), which simplifies things mathematically, but also implies that there are no losses or dispersion in the material. SHG is the result of a signal coming from the quadratic component of this polarization, and thus the properties and physics of the material itself will be encoded in the χ^2 tensor of third rank.
In a more formal description, the elements in the $\chi^{(2)}$ tensor are defined as the proportionality constants between the non-linear polarization components coming out of the sample P_i and the quadratic product of the incoming electric field components at a frequency ω_0:

$$P_i(2\omega_0) = \epsilon_0 \sum_{jk} \chi^{(2)}_{ijk}(2\omega_0; \omega_0)E_j(\omega_0)E_k(\omega_0) \tag{2.9}$$

Where the dependance on $2\omega_0$ in the polarization components comes from the product of the exponentials in the electric field components, i.e. $E_j = E_0e^{-i\omega_0 t}$. The main reference for this section is the book by Boyd [1].

The Lorentz model for an electron

As a first approximation to the problem, the Lorentz model of the electron as a classic harmonic oscillator is widely accepted method to find an expression for $\chi^{(2)}$. We need to solve the equation of motion for the electron exposed to the electromagnetic wave and make use of the usual definition for the polarization, $\vec{P}(\omega) = eN\vec{x}(\omega)$. Since the problem is not analytically solvable for all powers of the electric field, we will use a perturbative method where we will expand the electron's position around equilibrium [2]:

$$\tilde{x} = \tilde{x}^{(1)}\lambda + \tilde{x}^{(2)}\lambda^2 + \tilde{x}^{(3)}\lambda^3 + ... \qquad \lambda \in [0, 1] \tag{2.10}$$

We now will solve the equation of motion of the particle within an anharmonic potential. This is relevant for non-centrosymmetric media (like 2H phase TMDCs) which, as will be shown later, it is a necessary condition to have non-vanishing $\chi^{(2)}$

---

[2] This is a valid method as long as the wave frequency is away of any material resonance, and the deviation from the equilibrium position is small enough compared to the lattice constant in the material. It is similar to the method used in solving the Schrödinger equation in quantum mechanics' perturbation theory.

tensor components. We find a quadratic term in the force coming from the cubic contribution to the potential, giving it its non-symmetric shape, and in a more general case of two fields with frequencies ω_1 and ω_2 shining on the material (we will then turn into the SHG case where $\omega_1 = \omega_2$) we solve the equation of motion:

$$\begin{aligned} \ddot{\tilde{x}} + 2\gamma\dot{\tilde{x}} + \omega_0^2\tilde{x} + a\tilde{x}^2 &= -e\lambda\tilde{E}/m \\ \tilde{E}(t) &= E_1 e^{-i\omega_1 t} + E_2 e^{-i\omega_2 t} + c.c. \end{aligned} \tag{2.11}$$

Where the parameter λ determines the strength of the perturbation. We will now solve separately this equation for all the different contributions proportional to λ, λ^2, etc. From the coefficients linear in the parameter we can solve for the position $\tilde{x}^{(1)}$ as a classical lorentz model for the atom's position, with a steady-state solution:

$$\begin{aligned} \ddot{\tilde{x}}^{(1)} + 2\gamma\dot{\tilde{x}}^{(1)} + \omega_0^2\tilde{x}^{(1)} &= -e\lambda\tilde{E}/m \\ \tilde{x}^{(1)}(t) = x^{(1)}(\omega_1)e^{-i\omega_1 t} &+ x^{(1)}(\omega_2)e^{-i\omega_2 t} + c.c. \end{aligned} \tag{2.12}$$

Which for each ω_j contribution to the position results in:

$$x^{(1)}(\omega_j) = -\frac{e}{m}\frac{E_j}{D(\omega_j)} \tag{2.13}$$

Where we have defined the denominator $D(\omega_j) = \omega_0^2 - \omega_j^2 - 2i\omega_j\gamma$ for convenience, giving us the usual solution for a damped, driven harmonic oscillator in this first approach to the solution. Until now there is not much novelty, but there is as we turn into the equation stemming from the quadratic terms in λ:

$$\ddot{\tilde{x}}^{(2)} + 2\gamma\dot{\tilde{x}}^{(2)} + \omega_0^2\tilde{x}^{(2)} + a[\tilde{x}^{(1)}]^2 = -e\lambda\tilde{E}/m \tag{2.14}$$

And by making use of our solution for $\tilde{x}^{(1)}$, the squared term will introduce frequency contributions in $2\omega_1$, $2\omega_2$, $\pm(\omega_1 + \omega_2)$ and $\pm(\omega_1 - \omega_2)$. The latter two are known as sum and difference-frequency generation, respectively. For our purposes we will only focus in the first $2\omega_1$ contribution, for which we can solve the equation:

$$\ddot{\tilde{x}}^{(2)} + 2\gamma\dot{\tilde{x}}^{(2)} + \omega_0^2\tilde{x}^{(2)} = \frac{-a(eE_1/m)^2 e^{-2i\omega_1 t}}{D^2(\omega_1)} \tag{2.15}$$

And by looking for a steady-state solution $\tilde{x}^{(2)} = x^2 e^{-2i\omega_1 t}$ we find:

$$x^{(2)} = \frac{-a(e/m)^2 E_1^2}{D(2\omega_1)D(\omega_1)^2} \tag{2.16}$$

We are now in position of using the definition of the non-linear susceptibility (2.9) to identify the $\chi^{(2)}$ tensor:

$$\begin{aligned} P^{(2)}(2\omega_1) &= \epsilon_0\chi^{(2)}(2\omega_1, \omega_1, \omega_1)E^2(\omega_1) \\ P^{(2)}(2\omega_1) &= -Nex^{(2)}(2\omega_1) \end{aligned} \tag{2.17}$$

And by comparison of the two equations we find the result:

$$\chi^{(2)}(2\omega_1, \omega_1, \omega_1) = \frac{N(e^3/m^2)a}{\epsilon_0 D(2\omega_1)D^2(\omega_1)} \tag{2.18}$$

Even though the electron within a real life crystal behaves differently compared to a single electron in this simple potential, this example illustrates the concept of a second order signal coming from the system that is quadratic in the electric field. This is the essence of second harmonic generation processes, and now we will go over a more realistic description of the $\chi^{(2)}$ tensor.

Properties of the nonlinear susceptibility

We now turn our heads to a more realistic expression for $\chi^{(2)}$ and its properties, that will help us in the calculation of the components of the tensor. We will assume a case where two incoming fields with frequencies ω_1 and ω_2 interact to give a third frequency $\omega_3 = \omega_1 + \omega_2$. By the definition of the nonlinear susceptibility 2.9 but for this more general case of two different incoming frequencies[3]:

$$P_i(\omega_n + \omega_m) = \epsilon_0 \sum_{jk} \sum_{(nm)} \chi^{(2)}_{ijk}(\omega_n + \omega_m; \omega_n, \omega_m) E_j(\omega_n) E_k(\omega_m) \tag{2.19}$$

There are 12 possible tensors depending on the frequency contribution $\omega_n + \omega_m$. Since each third-rank tensor has 27 components (3 stacked 9x9 matrices), we have in the most general case a total of 324 complex components that describe the relation between the incoming fields and the outgoing polarization. However, we will now use the symmetries of the physics and geometry of the system to narrow down the independent components. It is very important that the excitation frequency is significantly far from the resonance frequencies of the material, which is our case since the our laser will have $\lambda = 1040$ nm (1.2 eV) and the closest exciton resonance lies at 1.9 eV.

This implies, on the one hand, that the components of the tensor are real, and on the other we can assume Kleinman's symmetry which implies that the nonlinear susceptibility is essentially independent of frequency. Furthermore, since we are far from resonance, the medium can be assumed to be lossless and this implies a permutation symmetry in the components of the tensor, which together with Kleinman's symmetry implies:

$$\chi^{(2)}_{ijk} = \chi^{(2)}_{jki} = \chi^{(2)}_{kij} = \chi^{(2)}_{ikj} = \chi^{(2)}_{kji} = \chi^{(2)}_{jik} \tag{2.20}$$

Which will simplify our lives significantly. For the exact values of these tensor elements we will need to consider the specific material. Furthermore, its crystal structure may impose further restrictions in the independent elements of the tensor, as explained next.

Influence of spatial symmetry on the nonlinear susceptibility

The material response to the incoming fields will be influenced by the internal spatial symmetries present in the crystal structure. We already saw in Table 2.1 that the number of layers in our MoS_2 sample will strongly influence its symmetry properties, including the presence of spatial inversion symmetry. From a physical perspective, if two directions are equivalent from a crystallographic point of view, the material response (i.e. the $\chi^{(2)}$ corresponding components) should be the same. Furthermore, a **centrosymmetric material will not show a nonlinear response to an incoming field**, and thus the $\chi^{(2)}$ tensor will be identically zero. This is a very general and powerful result, and backs up the idea of a nonlinear response ultimately stemming from the anharmonicity/asymmetry present in the atoms' motion within the crystal. We saw in table 2.1 that the bulk 2H phase belongs to the D_{6h} group, and thus it doesn't show spatial inversion symmetry. This means that it won't show any nonlinear response and thus the SHG signal will be zero. However, as soon as we find any kind of defect that brings back any kind of asymmetry (vacancies, edges, steps, etc.), we should recover the SHG signal. Since we will work with exfoliated TMDC multilayers, we expect SHG signal to be observed in many of these different kinds of defects.

---

[3] Here the notation (nm) implies that the subscripts *n* and *m* can be interchanged as long as the sum $\omega_n + \omega_m$ is kept unchanged. The frequencies can also be negative in this definition.

It is interesting to show the polarization dependance of the SHG intensity received in a 2H-TMDC monolayer. We have seen in Table 2.1 that it won't show any inversion symmetry and thus non-zero $\chi^{(2)}$ components. It has been reported a higher intensity of the signal when the incoming polarization is along any of the different zigzag directions [14], thus we can find an expression for the received intensity as:

$$I_{\|}(\theta) \propto cos^3(3\theta) \tag{2.21}$$

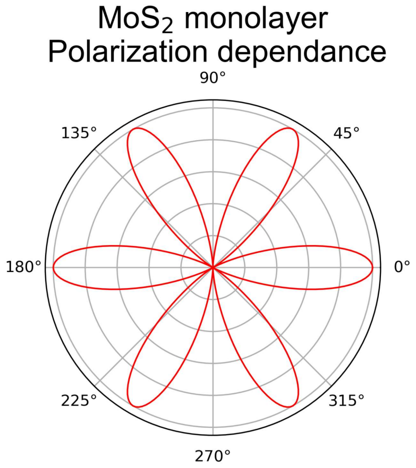

Figure 2.6: Polarization dependance for the normalized SHG signal intensity coming from an MoS_2 monolayer, showing higher intensity along the zigzag directions of the structure. It follows equation 2.21.

We should pay special attention to the edges, which are the main focus of this thesis. Translational symmetry is broken at the flake edge, and an immediate consequence is the reduction of the bandgap in the electronic structure of a 2H monolayer, compared to its 2D counterpart [23]. This will bring the excitation much closer to the electronic resonance, and thus the SHG signal will also be increased, and can be used to identify different types of edges and grain boundaries in some reported cases [12].

2.4 TMDC metamaterials with atomic precision

During this thesis we will focus our efforts on the study of a particular type of metasctructures that can be produced on TMDC multilayers, in particular MoS_2 and WS_2. These structures were first reported by Munkhbat B. et.al. [16] in 2020, and are produced by a combination of dry and wet etching on a 2H multilayer of TMDC, resulting in geometrical etched metastructures with high quality edges and hexagonal shape.

These structures are of particular importance, since they allow the production of high quality 1D defects at their edges, where the crystallographic and excitonic properties are highly respected. The etching process takes place in-plane and is highly anisotropic, producing zigzag-terminated edges, with geometric parameters predefined in the nanofabrication process. The growth of these metastructures only takes place on multilayer structures, and thus we will move away from the general tendency of the community to study monolayer TMDCs. These structures can be nanopatterned into arrays that show interesting photonic properties.

Even though the final etched structures have been well studied, the intermediate steps in the growth process is still not fully understood. The method is highly reproducible in WS_2, but for the case of MoS_2 we have observed variability from sample to sample, depending on the geometry of the structures and the etching conditions. This has motivated their study under different techniques, to further understand the growing mechanism and their suitability as a playground for edge physics.

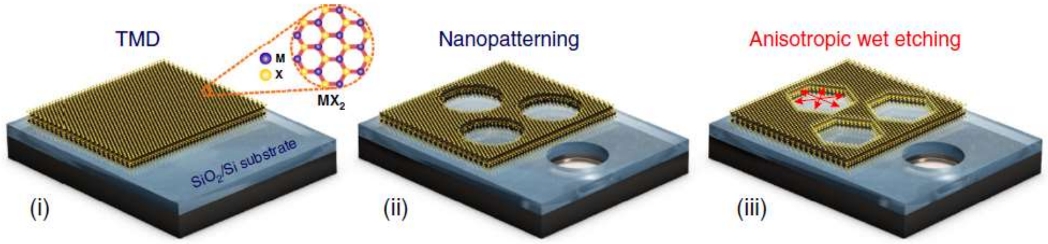

Figure 2.7: Scheme of the nanopatterning process taking place on the TMDC multilayer i) 2H-TMDC sample lying on SiO_2/Si substrate ii) flake is dry-etched via electron beam lithography into circular holes iii) wet etching turns circles into hexagonal metastructures ready to be studied. Adapted from [16].

Fig. 2.7 shows the different steps of the nanopatterning process, which will be further explained in detail in the Methods section 3.2. Here we observe how the in-plane anisotropic wet etching process produces hexagonal shapes following the zigzag directions of the crystal, producing 120º angles at the corners of the structure. This was thoroughly studied in the original paper by Munkhbat et. al. for WS_2 samples, leading to very high-quality edges with respected excitonic and optical properties. These structures could be further etched in different array fashions to

show photonic processes, or even to give shape to different nanostructures highly-controlled nanorribons.
For the case of MoS_2, though, recent experiments show a less well-defined outcome of the nanopatterning process, where adjacent layers don't follow the same etching directions and thus the inner walls of the hexagonal holes are not uniform. This motivated the study of these nanostructures on MoS_2 multilayers through different techniques, which is the main goal of this work. In Fig. 2.8 we can observe the good quality of the edges in the WS_2, while a different optical contrast is appreciated in alternating edges of the MoS_2 hexagon, which has a distorted geometry with these edges slightly shorter than the other three. The goal is to study these defects in detail via spectroscopic and mechanical characterization.

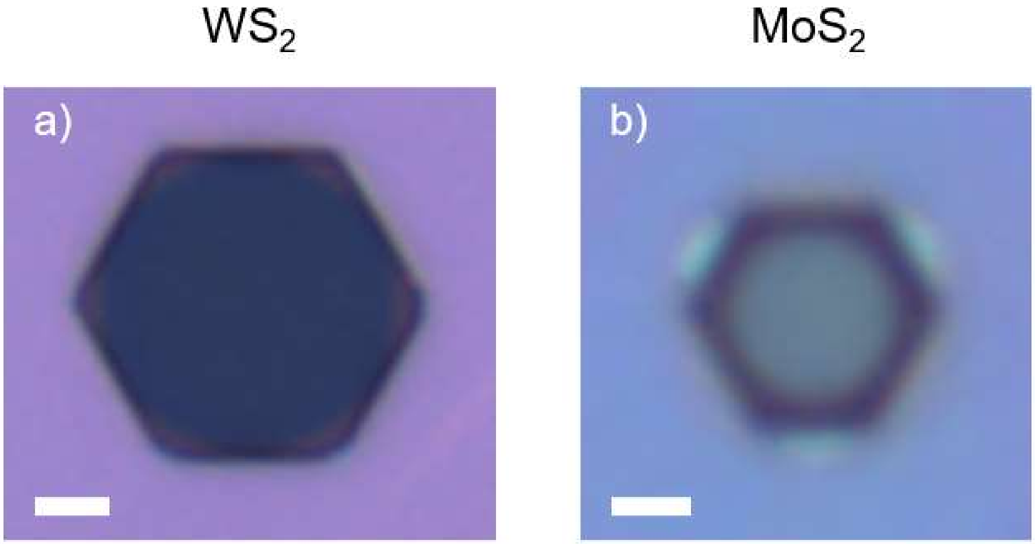

Figure 2.8: Optical images of produced metastructures on a) WS_2 (scalebar 5 um) and b) MoS_2 (scalebar 1 um) samples. It is observed a different optical contrast on alternating edges in the MoS_2 sample. The images were taken with a 100x/0.9 objective.

3

Methods

This section covers the details of the production, characterization and analysis methods used in the thesis. Going from a pristine, raw crystal to a metastructure etched down to atomic precision is a process with several steps, involving both physical and chemical processes. Next, extracting the information from the crystal via light-matter interactions requires precise set-up and calibration of Raman and SHG setups, making use of advanced optics and spectroscopy. Additionally, scanning electron (SEM) and atomic force (AFM) microscopies as complementary characterization techniques are introduced.

3.1 Sample preparation

Mechanical exfoliation: the layered nature of TMDCs and the relatively weak interaction between the layers, of the Van der Waals type, allow us to use a widespread mechanical top-down approach in order to isolate flakes of the desired lateral size and thickness. The method consists of, first, use a blue scotch tape to stick on the desired bulk crystal, and mechanically pull out a coarse portion of flakes that will itself be stuck to another blue scotch piece. The latter is called the '1st generation' of flakes.

Repeat the process on further blue scotch pieces, until we produce 4 generations of flakes. The subsequent 'stick and strip' process will provide us with thinner (but also smaller and less stable) flakes. Finally, take a scotch piece of the desired generation and stick it onto a polydimethylsiloxane (PDMS) stamp lying on a glass plate. Inspect under the optical microscope for the desired thickness and size of the flakes. Fluorescence microscopy will allow the precise identification of monolayers due to their direct bandgap.

In contrast with bottom-up methods like chemical vapour deposition (CVD) or molecular beam epitaxy (MBE), the resulting samples are of superior quality but smaller lateral size. That, together with the difficult control of how many exact layers we are able to extract from the bulk material, adds an inherent randomness to the process that we need to overcome by picking the appropriate flake.

Flake transfer to Si/SiO$_2$ sustrate: for the samples studied on such substrate, flakes need to be transferred from the PDMS stamp by the use of a micromechanical station, where the glass plate with the flakes on PDMS (facing downwards) is gently brought into contact with the new substrate (facing up). This is done while monitoring the process with an optical microscope, to make sure we transfer the desired flakes.

3.2 Metastructure production

To now etch the metastructures on our available TMDC flakes, a series of processes and reactions take place in a clean environment to prevent any potential contamination from the surroundings, as reported in [16]. For this, we made use of the ISO 5 Cleanroom at the Nanofabrication Laboratory at Chalmers University.

Electron beam lithography (EBL): the first step is to prepare a series of circular holes on a photoresist layer on top of our sample. For this, we spin-coat a layer of AR-P 6200.13 photoresist, at a speed of 2000 rpm and an acceleration of 250 rpm^2, followed by a soak baking at 130 ºC for 5 min. A design of the desired holes is then etched with an electron beam lithography system (JEOL JBX-9300FS), where the exposed part of the resist is degraded (positive resist). After the EBL process, the rest of the photoresist on the exposed areas is removed with Pentylacetate 99%.

Dry etching: we now introduce the samples into a plasma gun, where a plasma made from CHF_3 ionized gas will etch the exposed areas of our flakes for the desired time, at a rate of 10nm/min. This will ideally produce etched cylinders down to the SiO_2 layer, which will then stay exposed. The used plasma forward power was 50 W.

Wet etching: finally, we remove the remaining photoresist with NMP (1-methyl 2-pyrrolydone) and acetone, to then introduce the samples into a solution consisting of 100 mL of H_2O, 10 mL on NH_3 and 10 mL of H_2O_2, everything on a hotplate to control its temperature. The time we leave the sample in the solution will be mainly determined by the size of the holes we etched previously. The result of all this process will be a selection of metastructures on TMDC multilayers, with the desired size and depth. They can result into two shapes: regular hexagons and irregular ones with a more triangular shape (these only appear for small enough etching on MoS_2, see Fig. 3.1), depending on the material and etching conditions.

TMDC	**Etching time**	**Temperature**	**Metastructure**
WS_2	40 min	65 ºC	Hexagons
MoS_2	90 min	65 ºC (75 min) + 85 ºC (15 min)	Hexagons & triangles

Table 3.1: Experimental parameters for the growth of the metastructures to be studied in the experiments.

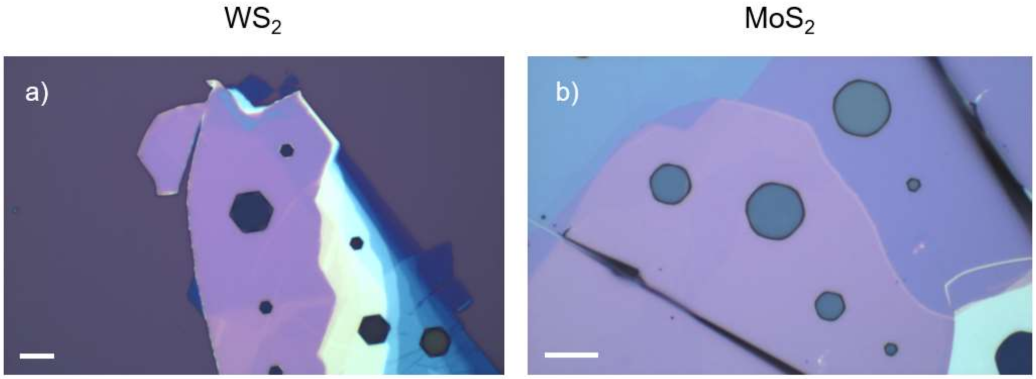

Figure 3.1: Types of produced metastructures with different diameters and flake thicknesses on a) WS_2 and b) MoS_2. We observe sharper edges on WS_2 samples and distorted hexagonal shapes on MoS_2. Scalebars 10 um.

3.3 Raman setup and data analysis

To extract the Raman spectra from our samples we used a commercial WITEC Alpha 300R Raman Microscope, set in reflection geometry (köhler illumination) under a λ = 532 nm excitation through a Zeiss 100x/0.9 objective. The power was set under 0.5 mW to avoid sample heating, and the achievable resolution was given by the diffraction-limited spot, which for these conditions is given by abbe's resolution equation at 296 nm.

The excitation wavelength was chosen as a widespread and accepted standard in the literature, and changing it would hinder our access to previous studies on TMDCs. In addition, this wavelength is far from exciton resonances of the material.

Calibration of the experiments was done with a silicon sample before each round of measurements. We would measure the 1st order peak position and the 2nd order peak height as a reference. After calibration, power would be set to a fixed value with a power-meter and then measurements could begin. Optimization of Raman signal depends mainly on the number of modes within the focus (i.e. Rayleigh range) of the laser beam, the integration time and the excitation power. A power of 0.5 mW would allow a strong enough signal without inducing peak shifts due to heating, and the focus would be optimized with the live measurement of the peaks height. Integration time would be set such that at least 10 CCD counts would appear on the Raman peaks, which would allow a proper fitting of its parameters (see below), thus a longer time would be redundant. This is of special importance for large area scans.

Raman parameters
Objective: 100x/0.9
Grating: 1800 g/mm
Spatial resolution: 296 nm
λ = 532 nm (CW)
P = 0.5 mW

With these parameters, the microscope allowed to perform single spectra on specific points, line scans along a predefined path, and area scans with a specific geometry.

In order to extract the physics from the raw data obtained from the light-matter interaction with the sample in the Raman setup described above, it is necessary to extract the parameters that properly quantify the Raman peaks observed on the obtained spectra. For this, I made use of a commonly accepted lorentzian fitting for the different vibrational modes.

Peak parameter extraction: to extract the peak position and width observed on the Raman spectra I made use of the `scipy.optimize.curve_fit` Python library to fit the obtained data to a lorentzian function, which I defined myself. This method uses a non-linear least-squares method to fit the data, and we only need to specify the bounds for the parameter space we want the fitting to converge in. Here is an example of fitting for the well-known silicon peak which is commonly used as substrate for our studied metastructures. The fitted Lorentzian function takes the shape:

$$I = \frac{I_0}{\pi\gamma\left(1 + \left(\frac{x-x_0}{\gamma}\right)^2\right)} \tag{3.1}$$

Where γ is a parameter giving the full width at half maximum (2γ = FWHM) and x_0 is the center of the peak. The output of this calculation are the optimized parameters as a four-element array `popt` and the corresponding covariance matrix `pcov`, from which we extract the parameter uncertainties. For this illustrating example on a Si/SiO$_2$ substrate, we obtain:

```python
# Define Lorentzian function with convenient parameters:
def lorentz(x,y0,amp,cen,wid):
    return y0 + (amp/np.pi)*(wid/((x-cen)**2 + wid**2))
# Perform fitting
a = 100             # Upper bound for background value y0
b = 1000            # Upper bound for peak height A
c = 550             # Upper bound for peak position x0
d = 50              # Upper bound for peak width w
popt,pcov = curve_fit(lorentz,x,y,bounds = ([0,0,500,0],[a,b,c,d]))
```

Peak position is 522.086 ± 0.005 cm^{-1}
FWHM is 7.10 ± 0.03 cm^{-1}

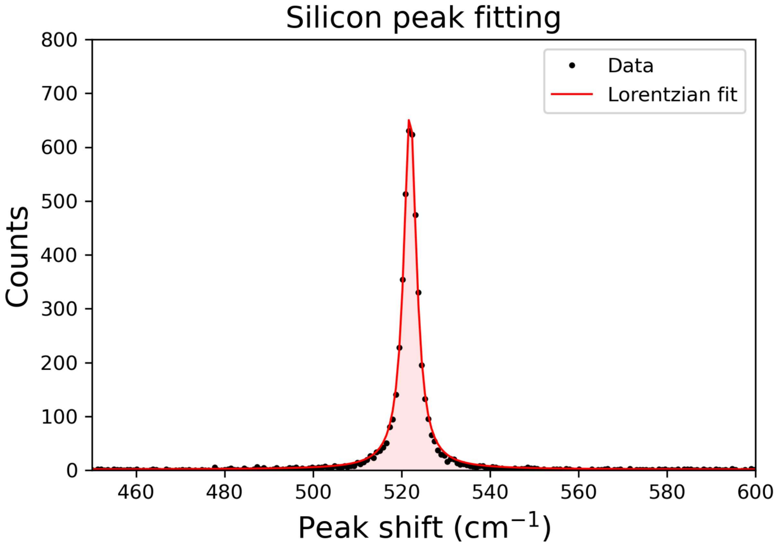

Figure 3.2: Silicon peak fitting example.

Image processing with extracted parameters: to obtain a simultaneous spectral and spatial distribution of the signal coming from the TMDCs, we performed an area scan over several structures encountered on our samples (edges, metastructures, steps, strained regions, etc.). This allows an easier correlation of the possible Raman signal modifications to the phenomena observed on the sample. With such a scan, we have a Raman spectra available for each point on the area scan that could later be processed.

For this post-processing, a Python script was developed to extract, sort and display the peak parameters we would require in each case. It goes over all the pixels on our scan, and performs a lorentzian fit explained above to all the relevant peaks observed on the available spectra. For a more reliable outcome, it also discards all the fitted parameters whose uncertainties surpasses certain values. This is important, since the convergence of the fitting requires a certain amount of counts on the peak from the setup CCD camera, and some features like edges or steps can't provide the same amount of counts as a flat surface. The script can still offer a value for the parameters, but for a large enough uncertainty, it has to be discarded.

3.4 SHG setup and data analysis

The strong electric field needed to induce nonlinear effects on the sample is achieved with a pulsed laser excitation at λ = 1040 nm and a pulse rate of 80 MHz and pulse duration of 100 fs, coming from a Ti:Sapphire femtosecond laser (MaiTai HP Newport Spectra-Physics). The wavelength (1.20 eV) is appropriate since it is far from the photoluminescence signal due to the MoS_2 excitons (around 1.8 eV).

The 1040 excitation goes first through a pair of polarizers that allow to both control its power and polarization direction, which we set to be parallel to the optical table, to reduce losses in the multiple reflections that take place along the setup. We then send the polarized, collimated signal through another pair consisting of a broadband polarizer (Thorlabs, WP25M-UB) and a half-wave plate (Thorlabs, SAHWP05M-700), in order to choose the polarization direction incoming on the sample by rotating the $\lambda/2$ plate[1].

SHG parameters
Objective: 40x/0.95
Detector: APD/Spectrometer
Spatial resolution: 547 nm
λ = 1040 nm (pulsed)
Excitation = 80 MHz/100 fs
P = 2-3 mW

The resulting light will feed the back aperture of a 40x/0.95 objective, focusing it to a 547 nm spot, scanning over the sample with a piezo stage (Mad City Laboratories, Nano LP200) in a reflection (epi) geometry. The second harmonic signal reflected from the sample, with λ = 520 nm, is then separated from the fundamental beam with a dichroic mirror[2] (Semrock, FF775-Di01-25 x 36) and a short-pass filter (Shemrock, FMM-720/SP-25) to be finally focused into a 50 um multimode fiber connected to either a spectrometer (Andor 500i, Newton 920 CCD camera) or an avalanche photo diode (APD) working as a single photon detector (APD, IDQ, ID100 Visible Single Photon detector), both connections allowed to analyze the quality of the signal and perform SHG mapping, respectively. The SHG setup is built on an optical table lying on pneumatic legs to reduce vibrations that may affect the results.

In order to check the quality and nature of the received signal, we send it into the spectrometer, where we expect the signal spectrum to show a peak at 520 nm. Furthermore, we also check that the power dependence of the received signal shows a slope of 2 in a logarithmic scale, for which the signal spectra was numerically integrated for different excitation powers. The setup also allows to obtain a bright-field image of the sample for reference and proper focusing of the laser spot onto the area we are interested in. A power of 2-3 mW allows enough SHG signal to get to the detector while avoiding sample heating or damage.

---

[1] The plate induces a phase change of π between the fast and slow components of the incoming electric field (with reference to the fast and slow axes in the birrefringent crystal), which will rotate the polarization direction by an angle of 2θ, where θ is the angle between the incoming polarization and the fast axis of the crystal in the plate. Thus, the rotation of the polarization plane is two times the angle indicated on the plate holder.

[2] A dichroic mirror has significantly different transmission and reflection coefficients for different wavelengths.

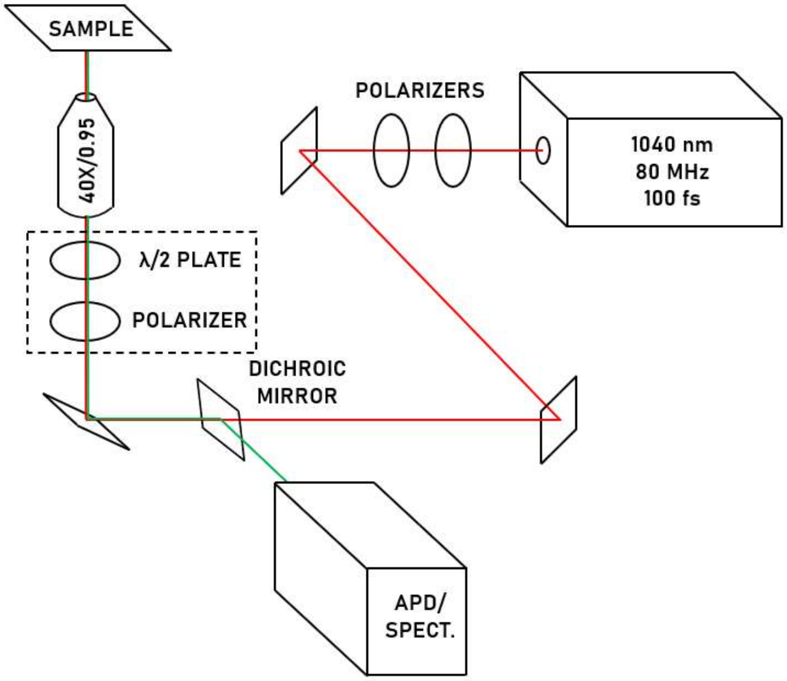
SAMPLE
40X/0.95
POLARIZERS
1040 nm
80 MHz
100 fs
λ/2 PLATE
POLARIZER
DICHROIC
MIRROR
APD/
SPECT.

Figure 3.3: SHG setup. The fundamental beam (1040 nm) is depicted in red, while the SHG signal (532 nm) is shown in green. The dashed box shows the elements that can be removed from the setup to make unpolarised measurements.

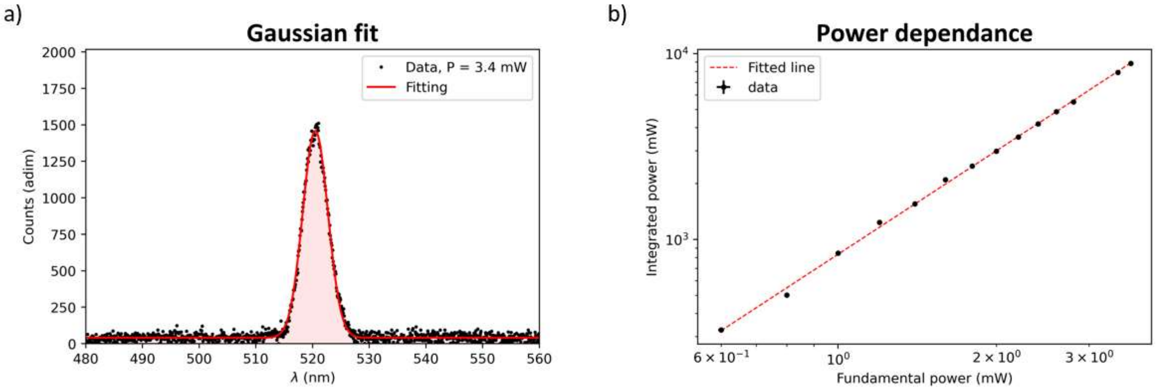

Figure 3.4: SHG signal verification. a) Gaussian fitting to the signal spectra, centered at 520 nm with double the frequency of the original 1040 nm excitation. b) Integrated power dependance of the fundamental power, showing a quadratic dependance in the logarithmic scale as expected.

The setup described above is suitable to measure the intensity component parallel to the incoming laser excitation $I(\theta)_{\parallel}$ in polarised measurements. This is possible since the rotation of the polarization plane of the field coming *into* the sample can be rotated by the $\lambda/2$ plate and thus the polarizer will always recover the intensity component of the field coming *from* the sample that is parallel to the original excitation. The reflection geometry follows the sequence:

$$\text{Laser} \xrightarrow{\text{LP}} E_\omega \xrightarrow{\lambda/2} E_\omega(\theta) \xrightarrow{\text{Sample}} \color{red}{P_{2\omega} \xrightarrow{\lambda/2} P_{2\omega}(-\theta) \xrightarrow{\text{LP}} I_{\parallel}(\theta)}$$

Where black text denotes radiation going *towards* the sample, and red text denotes radiation that goes *from* the sample towards the detector. Note that every rotation is done by the $\lambda/2$ plate. By performing the relevant math transforming the initial incoming field, and applying Kleinmann symmetry conditions in eq. 2.20 we obtain an expression for the parallel component of the intensity:

$$\begin{aligned} I_{\parallel}(\theta) = & |\chi^2_{xxx}cos^3\theta + 3\chi^2_{xxy}cos^2\theta sin\theta + \\ & 3\chi^2_{xyy}cos\theta sin^2\theta + \chi^2_{yyy}sin^3\theta|^2 \end{aligned} \tag{3.2}$$

Which will be measured by the APD in polarization-resolved experiments. By setting the symmetry conditions corresponding to the monolayer point group D$^1_{3h}$ (see Table 2.1) in the Kleinmann symmetry ($\chi_{xxx} = \chi_{xyy}$ and $\chi_{yyy} = -\chi_{xxy}$), we obtain the six-fold pattern shown in Fig. 2.21. The measured signal as a function of the angle will be fitted to eq. 3.2 in a similar procedure as for the Raman results, making use of the `scipy_optimize` library.

3.5 Additional characterization

To complement the Raman and SHG studies, we performed additional characterization on the metastructures by two imaging techniques: scanning electron microscopy (SEM) and atomic force microscopy (AFM), which allowed us to obtain additional information on the morphology and thickness of the structures.

SEM

This technique allowed us to obtain high-resolution images by the use of a focused beam of electrons, and is able to overcome the diffraction limit imposed by traditional optical microscopes. By the analysis of the backscattered secondary electrons from the sample, we were able to inspect the details around the edges of the metastructures and associate them to the different signals obtained from Raman and SHG spectroscopies. The operation of the microscope is based on a raster scan performed over the sample and a simultaneous analysis of the backscattered secondary electrons. This, together with the measured signal at each point, allows to convert the information into an image. The resolution is dictated by multiple factors, like the electron beam spot size, acceleration voltage or interaction volume within the sample, but can be as small as 1 nm.

The microscope used is a Zeiss Ultra 55 FEG located in the Chalmers Materials Analysis Laboratory (CMAL), which comprises a fully integrated energy and angle-selective electron detector. It allows an accelerating voltage of 20V - 30kV and a current probe of 4pA - 30nA, with a sample holder that allows a continuous 360° rotation and a tilt up to 70°.

AFM

This technique allows to image the topography of a sample down to atomic resolution, by bringing a tip close to its surface and tracking the tip-sample interactions over the surface. The distance is in the nanometer range, and thus relevant interactions include Van der Waals, electrostatic, chemical bonding forces or Pauli repulsion for short enough distances. A widely used potential to model the tip-sample interactions is the Lennard-Jones potential:

$$U_{LJ}(r) = 4U_0 \left[\left(\frac{R_a}{r} \right)^{12} + \left(\frac{R_a}{r} \right)^{6} \right] \tag{3.3}$$

That includes both repulsive and attractive forces for the tip-sample geometry. U_0 is the potential well depth and R_a is the distance at which the potential is zero.

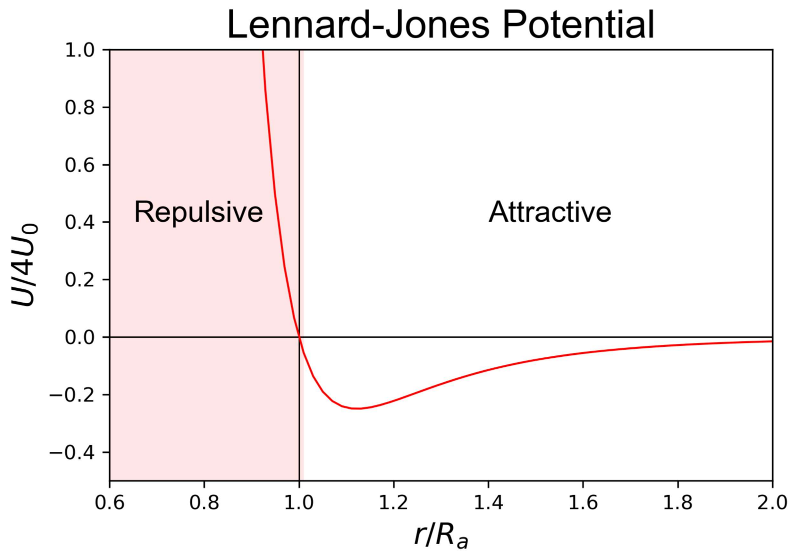

Figure 3.5: Lennard Jones potential, showing the attractive and repulsive zones at both sides of the equilibrium position for the tip-sample distance.

The tip is held by a flexible cantilever that is approached to the surface, and the distance is monitored by measuring the interferences of a laser focused in the back part of the cantilever. Like this, we are allowed to get both the distance and the phase of those interferences, and convert it into an image.
Our characterization was done with a commercially available Bruker Dimension 3100 AFM set in tapping mode.

4

Results and Discussion

4.1 Raman spectroscopy on WS_2 and MoS_2 samples

As a first proof of concept, Raman spectra were taken on TMDC samples prepared by mechanical exfoliation. Experiments were taken on bulk MoS_2 and WS_2, as well as on defects such as strained areas and their edges. The objective is to prepare the stage for later measurements on metastructures with a consistent check of previous results published in the literature.

Bulk TMDC samples

As described in Sec. 2.2, the 2H phase in bulk TMDCs are expected to show in-plane and out-of-plane vibrational modes at specific frequencies depending on the material. Our samples were exfoliated on PDMS and thus a spectrum of it was taken to check that no PDMS modes would affect our results. We confirm the expected peak positions for both samples, summarised in Table 4.1.

Bulk modes	E_{2g}	A_{1g}
WS_2	352.2 ± 0.2 cm^{-1}	417.3 ± 0.2 cm^{-1}
MoS_2	384.5 ± 0.2 cm^{-1}	409.8 ± 0.1 cm^{-1}

Table 4.1: Experimental results for the in plane (E_{2g}) and out-of-plane (A_{1g}) modes in bulk TMDC samples on PDMS.

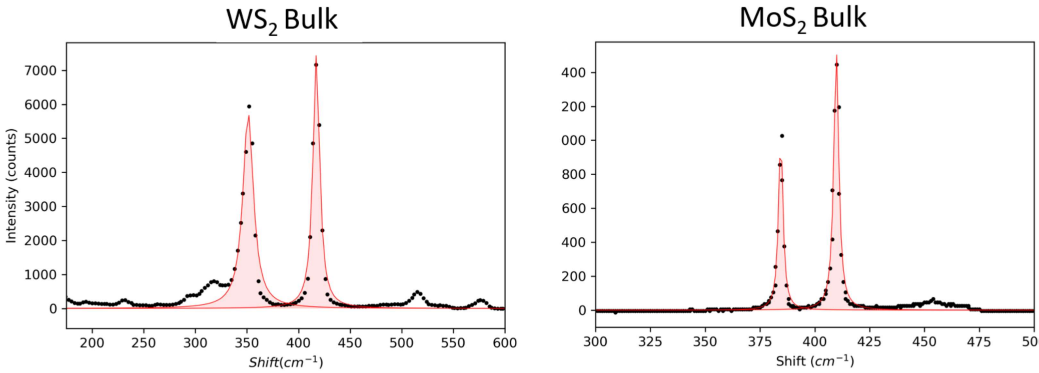

Figure 4.1: Raman spectra for bulk MoS_2 and WS_2. PDMS spectra shows no interference of the modes with the TMDC results.

Strain due to Transfer

The exfoliation process induces a non-isotropic strain on the sample, due to the many instabilities in the scotch tape method and the difficulties to control the direction of the pulling action. Another goal was to resolve this intrinsic strain through the in-plane mode, which is more susceptible to strain (see section 2.2). This is no easy task, since for an appreciable peak shift a strain above 1% is usually needed for a few-layer. For this, a zone where a strong ripple caused by the exfoliation process was located on a few-layer sample. Another complication is that if the ripple is too abrupt, the signal radiated by the exposed zone will not be directed back to the detector, and will be lost to the surroundings instead. Thus, the strain needs to be directed along the in-plane direction as much as possible.

In the right side of Fig. 4.2 we observe a mapping on WS_2 of the in-plane mode E_{2g} position over a scanned area where a ripple is observed and thus a strong in-plane strain is expected. The redshift due to tensile strain reported in the literature is confirmed in the areas where the optical constrast confirms to be the top of the ripple, and a tensile strain is expected to happen (white areas). On the other hand, at the valleys next to the ripples we observe the opposite behavior (darker areas). The measured position range is around 1 cm^{-1}, thus a good quality grating (1800/mm in our case) and a precise peak fitting procedure is needed to resolve this peak shift.

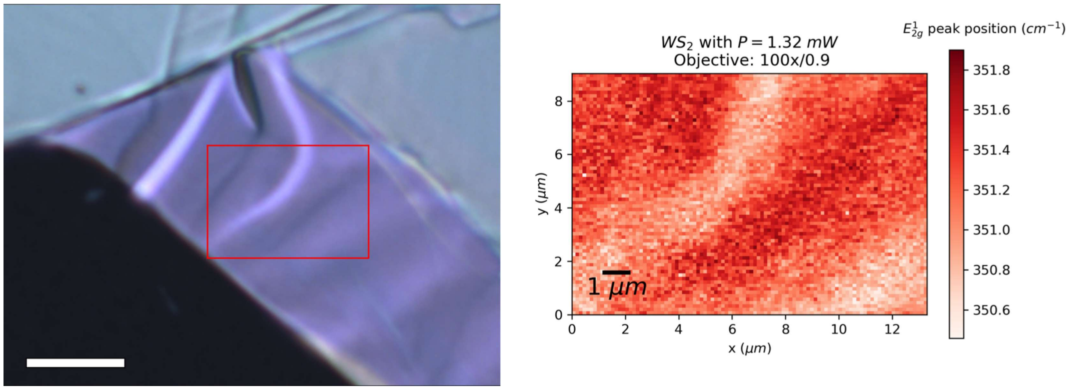

Figure 4.2: Optical image (left, scale bar 10 um) of a strained region on a few-layer WS_2 due to the exfoliation process, and Raman peak position map (right) showing the peak position of the in-plane mode E_{2g} the different positions on the red box on the optical image.

Thickness dependance

We have also seen that the Raman peak position is also dependent on the number of layers in the sample. In Fig. 4.3 we show measurements for both WS_2 and MoS_2 multilayer samples. For WS_2 we observe the expected blueshift for the in-plane mode for regions with less number of layers as we approach the flake edge. For a more quantitative check, individual spectra were taken on a MoS_2 sample, at two sites with evident thickness difference (see inset in Fig. 4.3 c), where the white region is bulk and the blue, smaller region only contains a few layers of TMDC). We observe the expected tendency for both modes, slightly more pronounced for the out-of-plane vibrations, see d).

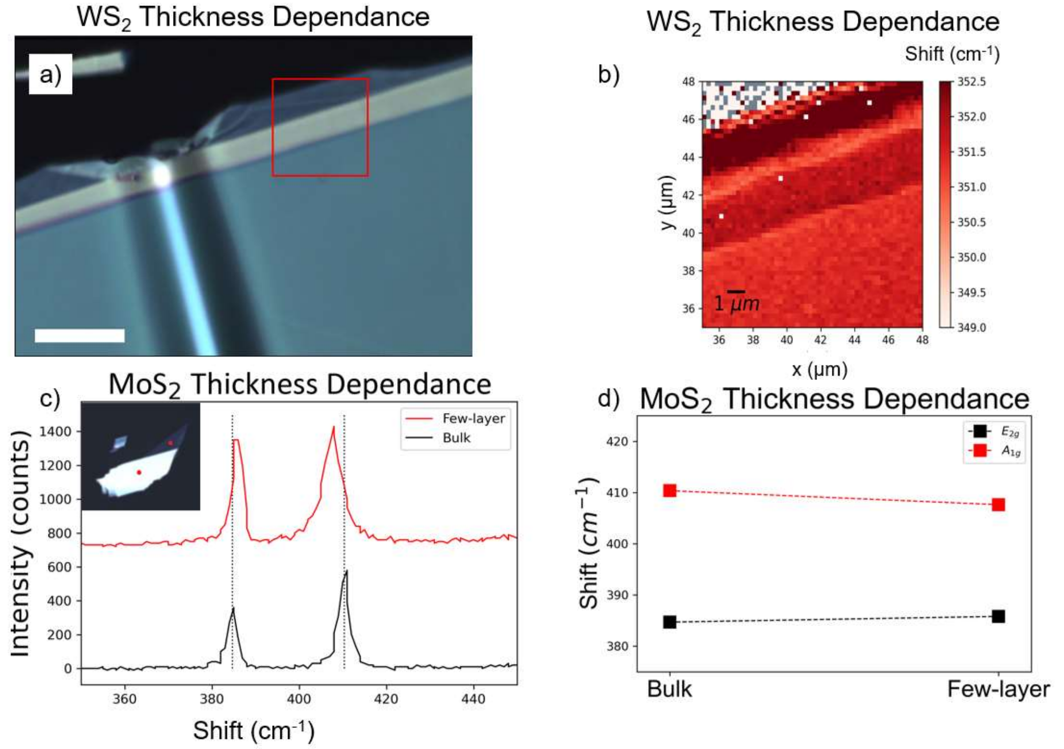

Figure 4.3: a) Optical image (scale bar 10 um) of a WS$_2$ multilayer region with several steps of different heights b) Raman peak position map showing the peak position of the in-plane mode E$_{2g}$ over the different positions on the red box on the optical image c) Raman spectra on two sites with different thickness on a MoS$_2$ sample seen on the inset (lateral size of image 10 um) d) Fittings for the peaks in c)

Raman spectra at the edge

It will be important for our purposes to check the vibrational quality of the edges at the hexagonal metastructures, and for that we will compare them with exfoliated flake edges, by checking if they show a significant shift. It is interesting to quantify if this shift is due to some strain mechanism or some structural change at the edge. For this, we perform different line scans along different edges, and we observe a systematic blueshift for both in-plane and out-of-plane modes as we approach the edge of the flake. This shift is very subtle (less than 1 cm^{-1}), but a bit more pronounced in MoS$_2$, thus we show the results for such a few-layer in Fig. 4.4. The studied edge is shown in a) and the fittings for all the peaks seen in the spectra in c) are shown as a function of the position along the linescan in b) and d).

These results are in line with previous characterizations of 2D-TMDC edges [19], where a highly-localized strain within 2 nm from the edge was detected. This hardening of the edge may be the cause for the vibrations to travel with an increased frequency shift in its vicinity.

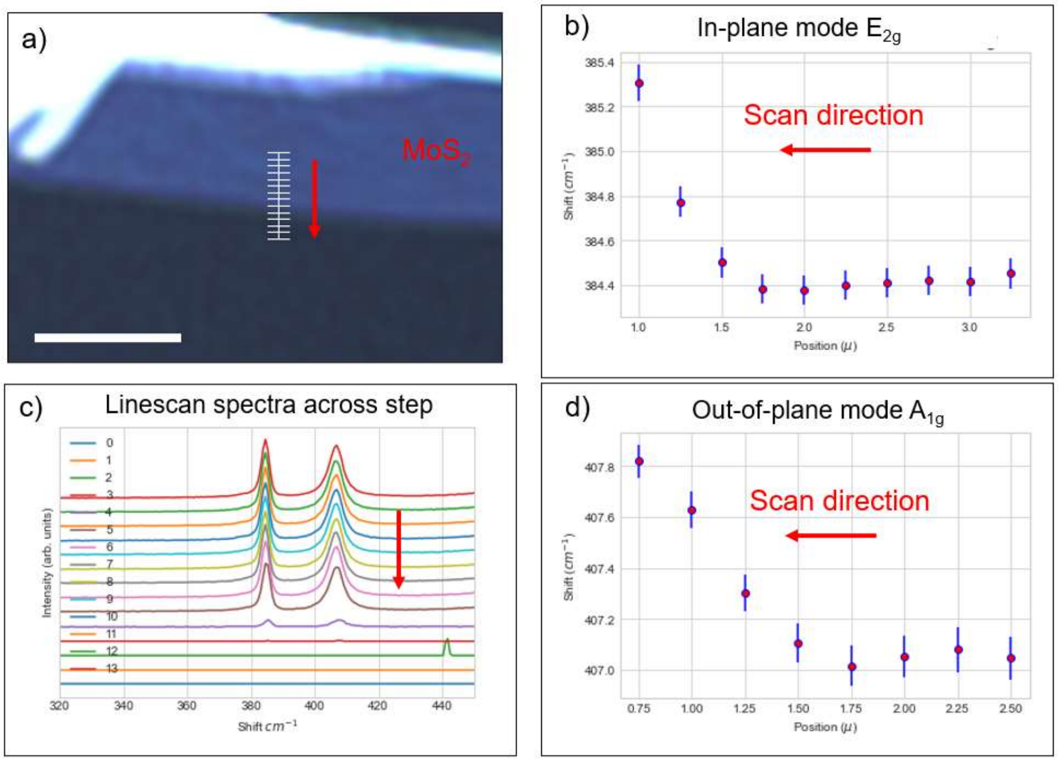

Figure 4.4: Line scan across flake edge a) optical image of the scanned edge, with the red arrow denoting the scanning direction from inside the flake towards the outside (scale bar 5 um) b) d) fitting of the Raman peaks for both in-plane and out-of-plane modes, respectively c) spectra taken at all the points along the scan.

4.2 AFM and SEM

We now get into the study of the etched metastructures, whose production process was outlined in section 3.2. This work is focused on MoS_2 samples, motivated by the fact that previous work done on this material showed that the etching process can result in triangular structures compared to the more defined and understood hexagonal ones that grow on WS_2.

For a detailed visualization of the metastructures, we used advanced microscopy techniques. SEM allowed us to directly observe the hexagon morphology on MoS_2 flake. In Fig. 4.5 a) we see four different hexagons with diameters 2, 5, 7 and 10 um, and all of them have edges that are not as sharp as what we saw on WS_2 optical images in Fig. 2.8. These images allow us to appreciate how all layers' etching still follows the zigzag directions as in WS_2, but the individual layers penetrate further in-plane pushing three of the hexagon edges, trying to obtain a triangular shape. Furthermore, not all layers are etching through the same set of edges, as we can appreciate in Fig. 4.5 b), which shows the edges of the top layers highlighted in a red, dashed line for the 2 um hexagon. Fig. 4.5 c) shows the same structure, but with a higher accelerating voltage that allows to image the underlying layers, and we see how the other trio of edges are the ones with a more advanced in-plane etching. The edges at the top layers of the sample are still highlighted for visual guidance, see Fig. 4.5 d).

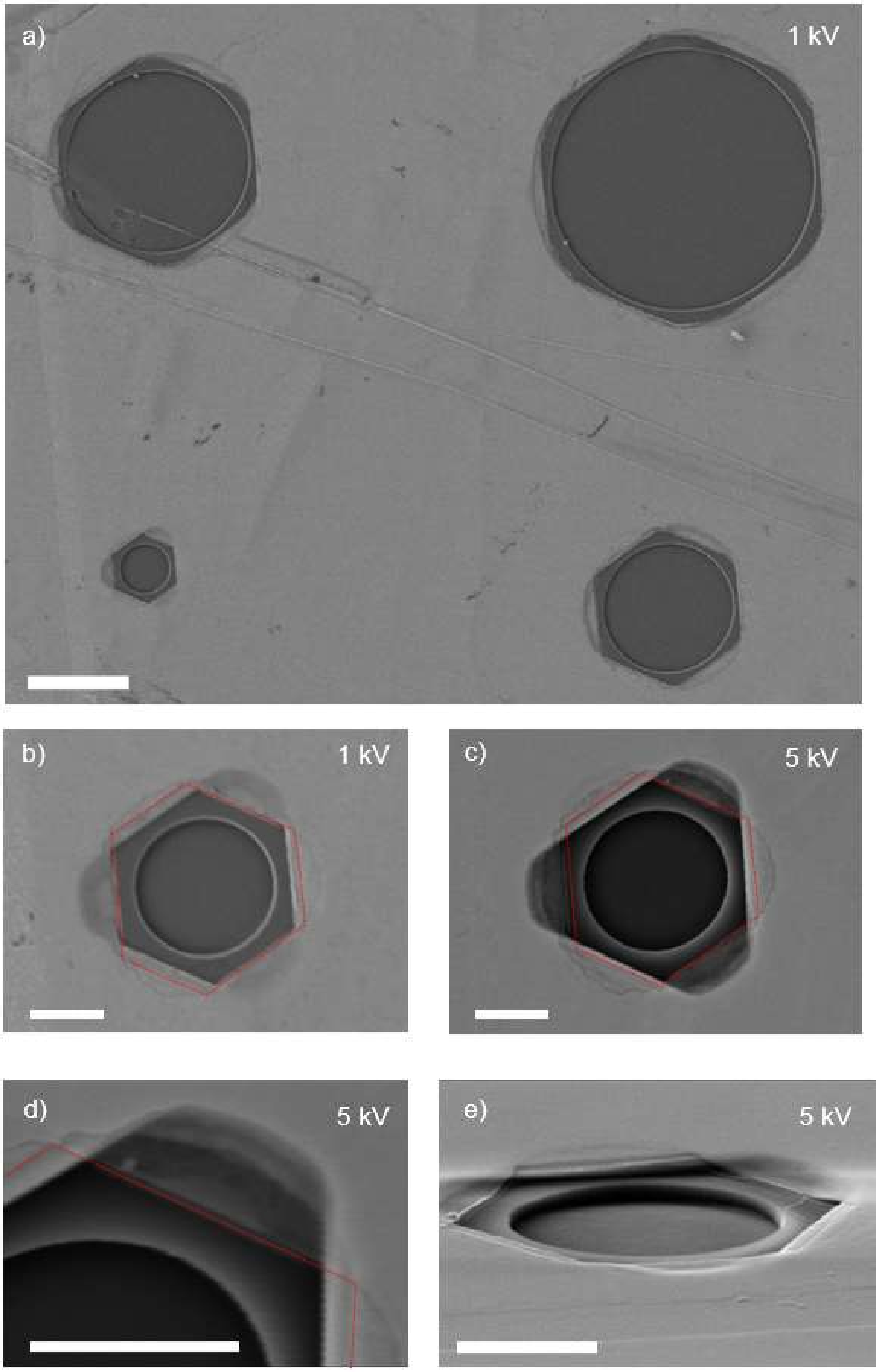

Figure 4.5: SEM images. a) Collective vision of all the structures (scalebar 5um) b) 2um hexagon at 1 kV acceleration voltage, showing the topmost layers c) 2 um hexagon at 5 kV acceleration voltage, showing the layers beneath the topmost layers d) enlarged vision of c) at the top-left edge e) tilted vision of the 2 um structure, clearly showing the depleted regions at the three alternating edges due to the absence of material beneath it.

But the most enlightening result is in Fig. 4.5 e), where a tilted image of the structure clearly shows how the top layers are bending over the space that the missing layers beneath it have left after their more advanced in-plane etching. Finally, we also see in all the images how the topmost layer undergoes a more irregular etching than the ones immediately beneath it, probably due to the greater exposure to the liquid solution that produces the etching (the layers beneath are only exposed directly at the edge).

AFM results in Fig. 4.6 a), b) show the same 2 um structure, with linescans along the two different types of edges. Fig. 4.6 c) shows the amplitude profile for the edge where the topmost layers show a most pronounced etching, and the inset shows the step formed between poitns A and B. This step is sharp and of a thickness of 10 nm, again confirming that it is not a single layer but a few-layer stack, since one layer has a thickness of 0.3 nm. We also observe a progressive amplitude increase as we go past point A to the left, which confirms an etching of lower quality for the most exposed layers at the top of the flake.
In Fig. 4.6 d) we see a progressive, pronounced amplitude decrease between points A and B of height 50 nm, before the edge of the TMDC. This confirms that below the topmost few-layer stack that we studied in c), there is no TMDC present due to a more advanced etching, which causes a depletion region of 0.5 um before the edge. We can also see a small bump at the very edge at point B. This suggests that the point of contact is done right before the terminal atoms at the edge.

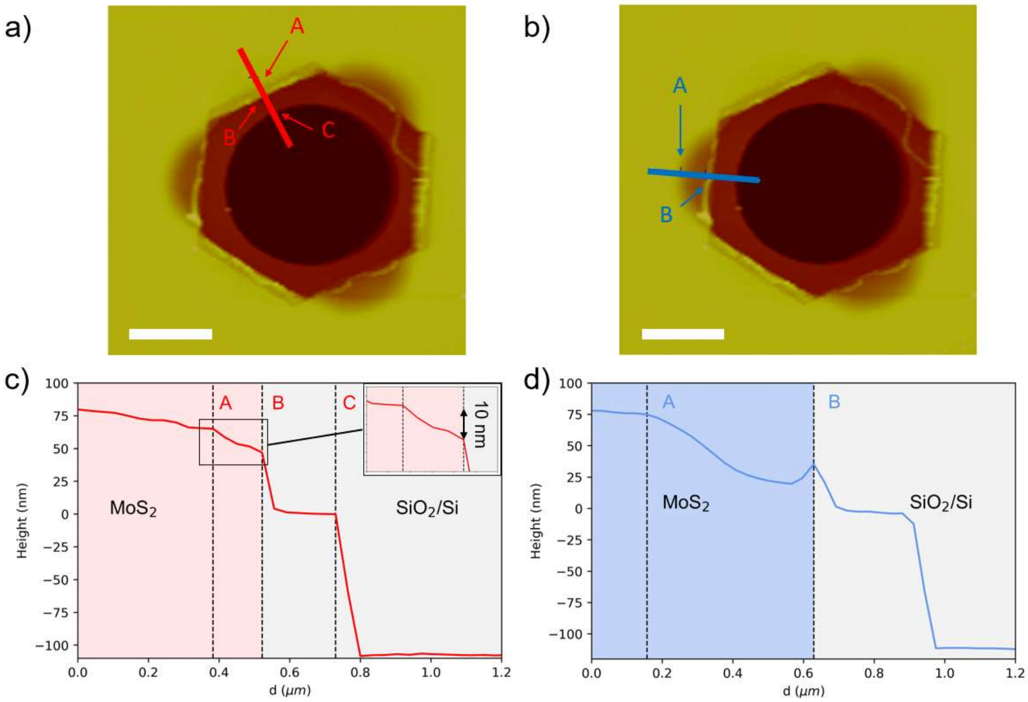

Figure 4.6: AFM images. a) b) AFM scans of the 2 um structure, whowing contrast for the differently etched edges (scalebars 2 um) c) amplitude section for the red line in a) d) amplitude section for the red line in b).

4.3 Raman Spectroscopy on MoS_2 Metastructures

We now turn our heads towards spectroscopic measurements of the 2 um metastructure. Fig. 4.7 shows the results of Raman spectroscopy performed around a 2 um diameter hexagonal metastructure. The depleted regions show a peak redshift in both modes at the sites corresponding to the lighter edges, see 4.7. b). The full-width at half maximum (FWHM) of the out-of-plane mode is displayed in c). Individual spectra are shown in d) and e), showing the peak shift between a region far from the metastructure and one of the depleted edges, the latter showing a redshift of 0.5 cm^{-1}, together with an increase of the detected counts of a 100% and a FWHM increase of 1 cm^{-1}. Note that the resolution of the laser (0.3 nm) is not enough to resolve a substantial difference at steps taking place at the other three edges, thus we can assume that the vibrational properties of the flake are well respected up until the edge of the hexagon at those locations.

The redshift at the depleted edges can be due to an increased strain at those regions, since a similar behavior was observed in previous studies (see Sec. 2.2). Also, an increased FWHM suggests that the total signal is comprised of both unstrained and strained vibrations within the laser focus, convoluted in a single peak of slightly larger width due to their different positions.

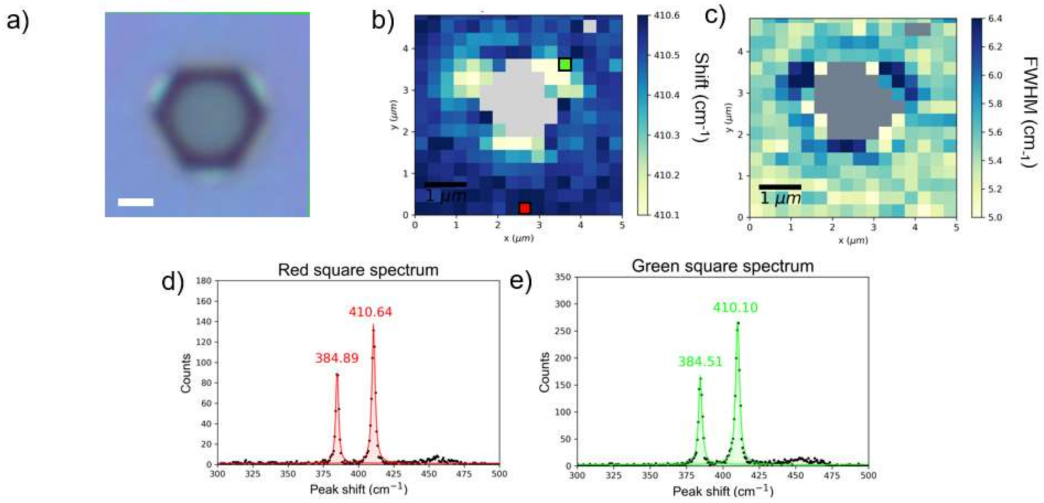

Figure 4.7: Raman spectroscopy around MoS_2 hexagonal metastructure a) Optical image of the etched structure with a 2 um diameter (scalebar 1 um) b) Raman scan around the metastructure, showing lower frequencies with lighter colors c) FHWM map of the area d) Raman spectrum performed at the red square, far from the structure. e) Raman spectrum performed at the green square, exactly at the redshifted area. Peaks are labeled with their shift position.

4.4 Second harmonic generation on MoS_2 metastructures

Second harmonic scans were performed over the hexagonal metastructures grown on MoS_2 to further characterize the edges studied in section 4.3. Polarised and unpolarised measurements were performed to isolate the different factors that may influence the results.

Unpolarised measurements

Fig. 4.8 a) shows an unpolarised SHG scan over a 60x60 um area, covering four metastructures with different diameters, and other defects in the sample like zones with different thicknesses or the sample edge. The log scale helps to visualize the regions with different thicknesses, and clearly shows the higher intensity at the edges.

The different hexagonal metastructures all show an increased SHG intensity at their edges, but the 2 um diameter one clearly shows very intense signal at the depleted edges, (see Fig. 4.8 b)) where we observed the Raman redshift in section 4.3. This depletion causes a substantial structural difference at those locations, producing a strong symmetry breaking, and thus non-zero nonlinear tensor components, causing a significant signal increase of more than an order of magnitude compared to the other edges, and more than 4 compared to the bulk.

Furthermore, we preivously confirmed with AFM that the suspended TMDC is not a monolayer, thus the signal increase can't be caused by a different crystal structure.

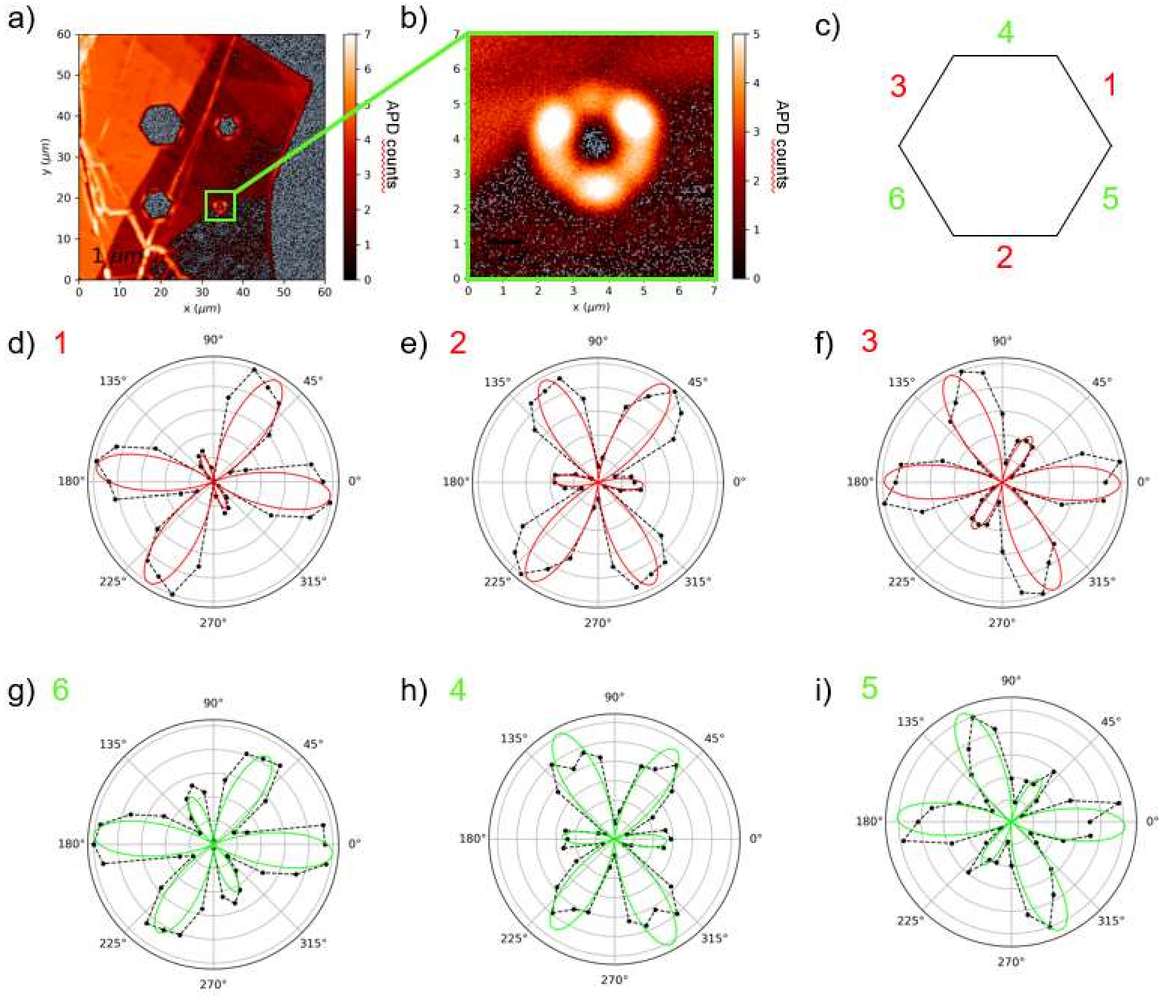

Figure 4.8: SHG scans around MoS_2 hexagonal metastructures with different diameters (left) and zoomed around the 2 um diameter structure studied with Raman Spectroscopy. Both panels are shown in log scale for better interpretation of the results. We observe a clear signal increment at the edges, especially at the ones that showed a raman redshift.

Polarised measurements

We then performed polarization-dependent measurements on the individual edges, making a difference between depleted (1,2,3, red) and non-depleted (4,5,6, green) edges, see Fig. 4.8 c). We observe a usual six-fold pattern for monolayer TMDCs (see Fig. 2.6), but with one direction with suppressed intensity. The suppressed direction shows the orientation of the exposed edge, since the other two zigzag directions showing an increase of the signal are equivalent by crystal symmetry.

The results' general shape is well fitted by eq. 3.2,, see **??**, yet many points at the

Depleted	**Edge 1**	**Edge 2**	**Edge 3**
χ_{xxx}	1.00 ± 0.04	1.00 ± 0.05	0.50 ± 0.08
χ_{xxy}	-0.30 ± 0.05	0.00 ± 0.08	-0.25 ± 0.05
χ_{xyy}	-0.76 ± 0.05	-0.86 ± 0.06	-0.97 ± 0.03
χ_{yyy}	-0.20 ± 0.04	0.15 ± 0.06	0.28 ± 0.06

Non-depleted	**Edge 4**	**Edge 5**	**Edge 6**
χ_{xxx}	0.99 ± 0.05	0.69 ± 0.08	1.00 ± 0.04
χ_{xxy}	-0.12 ± 0.05	-0.14 ± 0.06	-0.25 ± 0.05
χ_{xyy}	-0.85 ± 0.04	-1.00 ± 0.04	-0.87 ± 0.04
χ_{yyy}	0.38 ± 0.06	0.20 ± 0.07	0.01 ± 0.07

Table 4.2: $\chi^{(2)}$ components values for the fittings at the polarised measurements shown in Fig. 4.8.

bigger lobes don't follow the trend perfectly, which can be due to the low intensity used to prevent sample heating. The tendency is repeated for both depleted and non-depleted edges, and parallel edges display the same suppressed direction. This suggests that, even though the in-plane etching of the two sets of edges is done in different directions, the overall geometry of the topmost layers exposed to the excitation is still respected and the only difference is the depletion due to the absence of material beneath some edges.

These results suggest that the etching taking place under the topmost layers is of very good quality, and thus we can confirm that the wet-etching taking place on MoS_2 does not take place along the same directions for all the layers exposed to the solution, but it is still highly anisotropic and respects the geometry of the multilayer crystal structure. This is in big contrast with WS_2, where Munkhbat B. et. al. showed that the hexagons took place along the entire multilayer down to the substrate as a final, stable structure. SEM images in Fig. 4.5 a) show that larger metastructures show a similar behavior, but with a less advanced etching depth at all the edges due to the larger amount of material to react with the solution. This suggests that, if the etching were to continue for long enough time, or for smaller structures the final structure would be a triangle, which is also compatible with the fact that zigzag directions make 60º angles between them, making the hexagon not the only geometrical option for this etching process' outcome, see Fig. 4.9. the good quality of the etching crystal and the etching process makes the two triangles to maintain the same relative angle of 60º. However, smaller structures are not resolved by the spectroscopic techniques we have used here, thus 2 um was the best tradeoff between a reasonable time to observe an advanced state of the etching, while being accessible with Raman and SHG.

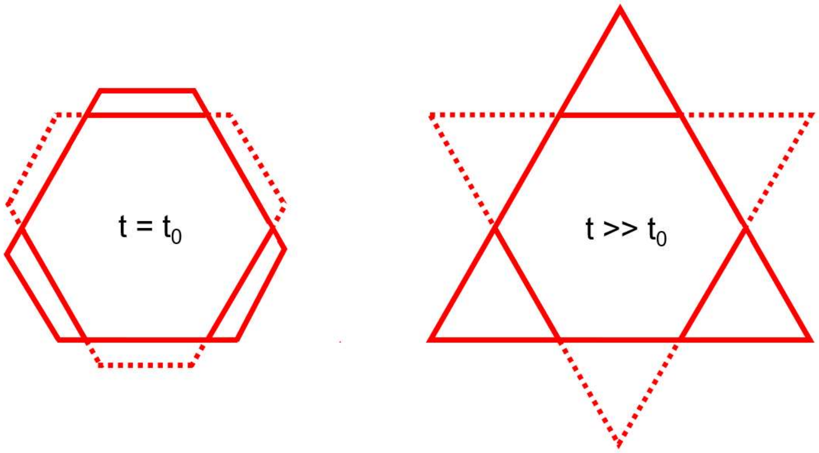

Figure 4.9: Etching process in MoS_2 samples. On the left we have the current situation of the studied metastructure, and on the right we have the proposed structure for a long enough time, when the etching process has removed all the material to make two adjacent triangles. Dashed lines show the shape of the triangle beneath the top layer.

5

Conclusions and Outlook

In this thesis, a physical system consisting on an etched hexagonal metastructure on multilayer Transition Metal Dicalchogenides was produced and characterised with spectroscopic and mechanical techniques, in particular Raman and Second Harmonic Generation spectroscopies, Scanning Electron Microscopy and Atomic Force Microscopy. The process covers the production of the structures from a pristine, bulk MoS_2 crystal, to an etched hexagonal structure down to atomic precision. The characterization was performed with both commercially available and assembled setups, in order to get a broader picture of the strain and edge physics taking place around these novel metastructures. The performed techniques allowed us to establish a solid correlation between the extracted data from light-matter interactions, and a physical interpretation regarding the vibrational properties, geometry and quality of the growth process of the hexagons.

A preliminary study of the multilayers was done via Raman spectroscopy, to check the vibrational properties of the samples as a function of the number of layers, strain, and vicinity to the edges. Next, SEM and AFM results allowed us to make a difference between two sets of edges around the hexagons on MoS_2, as well as Raman spectroscopy based on the shift observed on top of such edges, where both in-plane and out-of plane vibrational modes provided a suitable tool to track and correlate strain-related physical phenomena around the hexagons. These results are backed up by the SHG measured both by polarised and unpolarised measurements, which show an increase of the SHG signal at the depleted areas, but the same polarization-dependent tendency for both types of edges. Based on the obtained results, we conclude that WS_2 multilayer hexagons present edges that follow the same zigzag direction all the way down to the substrate, in contrast with MoS_2, where alternating few-layer stacks tend to develop into triangles 60º rotated with respect to each other. The geometry of the individual triangles is respected and of good quality, which suggests that the etching is still highly anisotropic and of very good quality, following the highly stable zigzag directions. This arrangement makes some layers to stay suspended on top of the vacant space left by the adjacent ones, which induces a geometry change in the crystal, with the subsequent straining of the layer and edge. As a consequence, we can conclude that WS_2 metastructures are a better option for studying physical phenomena taking place at the edges rather than MoS_2.

This thesis leaves room for further work though, since some experiments could not be carried out due to time constraints. Regarding the suitability of hexagons as a proper system for studying edge-related physical phenomena, a further characterization of WS_2 edges is needed, since in this thesis we focused on the understanding of the differences between MoS_2 and WS_2 hexagons. With respect to SHG expeirments, a higher fundamental power is recommended, since the problem of sample heating is more crucial for Raman experiments to prevent unwanted peak shifts, but in the case of SHG it would only improve the signal-to-noise ratio and the numerical fittings. Furthermore, and with eyes on future applications of these novel metastructures, it is interesting to perform similar characterization experiments on more elaborate metamaterials consisting of arrays of hexagons, honeycomb and bowtie layouts, nanorribons, etc., the only limitation is the optical diffraction limit imposed by such techniques, which prevents the structures from being too small and would increase the production time significantly.

Bibliography

[1] R.W. Boyd and D. Prato. *Nonlinear Optics*. Elsevier Science, 2008. ISBN: 9780080485966.

[2] "Classical Theory of Rayleigh and Raman Scattering". In: *The Raman Effect*. John Wiley Sons, Ltd. Chap. 3, pp. 31–48. ISBN: 9780470845769. DOI: `https://doi.org/10.1002/0470845767.ch3`.

[3] M Dadgar et al. "Achieving large, tunable strain in monolayer transition-metal dichalcogenides". In: *arXiv preprint arXiv:1705.05412* (2017).

[4] Saptarshi Das et al. "Transistors based on two-dimensional materials for future integrated circuits". In: *Nature Electronics* 4.11 (2021), pp. 786–799.

[5] Daphne Davelou et al. "Nanoribbon edges of transition-metal dichalcogenides: Stability and electronic properties". In: *Physical Review B* 96 (Oct. 2017). DOI: `10.1103/PhysRevB.96.165436`.

[6] Ying Ding et al. "Raman tensor of layered MoS_2". In: *Optics Letters* 45.6 (2020), pp. 1313–1316.

[7] Karel-Alexander N Duerloo, Yao Li, and Evan J Reed. "Structural phase transitions in two-dimensional Mo-and W-dichalcogenide monolayers". In: *Nature communications* 5.1 (2014), pp. 1–9.

[8] Jason K Ellis, Melissa J Lucero, and Gustavo E Scuseria. "The indirect to direct band gap transition in multilayered MoS_2 as predicted by screened hybrid density functional theory". In: *Applied Physics Letters* 99.26 (2011), p. 261908.

[9] Guoxiang Hu et al. "Superior electrocatalytic hydrogen evolution at engineered non-stoichiometric two-dimensional transition metal dichalcogenide edges". In: *Journal of Materials Chemistry A* 7.31 (2019), pp. 18357–18364.

[10] Sridevi Krishnamurthi, Mojtaba Farmanbar, and Geert Brocks. "One-dimensional electronic instabilities at the edges of MoS_2". In: *Physical Review B* 102.16 (2020), p. 165142.

[11] Rahul Kumar et al. "Transition metal dichalcogenides-based flexible gas sensors". In: *Sensors and Actuators A: Physical* 303 (2020), p. 111875.

[12] Kuang-I Lin et al. "Atom-dependent edge-enhanced second-harmonic generation on MoS_2 monolayers". In: *Nano letters* 18.2 (2018), pp. 793–797.

[13] Kin Fai Mak et al. "Atomically thin MoS_2: a new direct-gap semiconductor". In: *Physical review letters* 105.13 (2010), p. 136805.

[14] Lukas Mennel, Matthias Paur, and Thomas Mueller. "Second harmonic generation in strained transition metal dichalcogenide monolayers: MoS_2, $MoSe_2$, WS_2, and WSe_2". In: *APL Photonics* 4.3 (2019), p. 034404.

[15] Feng Miao, Shi-Jun Liang, and Bin Cheng. "Straintronics with van der Waals materials". In: *npj Quantum Materials* 6.1 (2021), pp. 1–4.

[16] Battulga Munkhbat et al. “Transition metal dichalcogenide metamaterials with atomic precision”. In: *Nature communications* 11.1 (2020), pp. 1–8.

[17] Kostya S Novoselov et al. “Electric field effect in atomically thin carbon films”. In: *science* 306.5696 (2004), pp. 666–669.

[18] Satyaprakash Sahoo et al. “Temperature-dependent Raman studies and thermal conductivity of few-layer MoS_2”. In: *The Journal of Physical Chemistry C* 117.17 (2013), pp. 9042–9047.

[19] Miguel Tinoco et al. “Strain-dependent edge structures in MoS_2 layers”. In: *Nano letters* 17.11 (2017), pp. 7021–7026.

[20] R. Loudon W. Hayes. “Scattering of Light by Crystals”. In: *Scattering of Light by Crystals*. John Wiley Sons, Ltd, 1978. ISBN: 9780486161471.

[21] Willes H Weber and Roberto Merlin. *Raman scattering in materials science*. Vol. 42. Springer Science & Business Media, 2000.

[22] Shao-Long Xiao, Wen-Zhe Yu, and Shang-Peng Gao. “Edge preference and band gap characters of MoS_2 and WS_2 nanoribbons”. In: *Surface Science* 653 (2016), pp. 107–112.

[23] X Yin et al. “O, Brien, K.; Hone, JC; Zhang, X. Edge Nonlinear Optics on a MoS_2 Atomic Monolayer”. In: *Science* 344.6183 (2014), pp. 488–490.

[24] X Zhang et al. “Raman spectroscopy of shear and layer breathing modes in multilayer MoS_2”. In: *Physical Review B* 87.11 (2013), p. 115413.

A

Appendix: SHG intensity derivaiton

Following the sequence defined in 3.2, we will follow the transformation of an incoming electric field with a fixed polarization along the $\hat{x}$ direction, which is rotate by the half-wave plate by an angle θ through the rotation matrix $T(\theta)$. We assume a reflection geometry, and thus vanishing z components in the fields and the $\chi^{(2)}$ tensor-related elements.

$$E_\omega = \begin{pmatrix} 1 \\ 0 \end{pmatrix}; \qquad T(\theta) = \begin{pmatrix} cos\theta & -sin\theta \\ sin\theta & cos\theta \end{pmatrix}; \qquad R_\omega(\theta) = T(\theta)E_\omega \tag{A.1}$$

And by equation 2.9 we obtain for the induced components at frequency 2ω out of the material:

$$\begin{aligned} P_{2\omega}(\theta) &= \begin{pmatrix} \chi_{xxx}R^x_\omega(\theta)R^x_\omega(\theta) + \chi_{xyy}R^y_\omega(\theta)R^y_\omega(\theta) + \chi_{xxy}R^x_\omega(\theta)R^y_\omega(\theta) + \chi_{xyx}R^y_\omega(\theta)R^x_\omega(\theta) \\ \chi_{yxx}R^x_\omega(\theta)R^x_\omega(\theta) + \chi_{yxy}R^x_\omega(\theta)R^y_\omega(\theta) + \chi_{yyx}R^y_\omega(\theta)R^x_\omega(\theta) + \chi_{yyy}R^y_\omega(\theta)R^y_\omega(\theta) \end{pmatrix} \\ &= \begin{pmatrix} \chi_{xxx}cos^2\theta + (\chi_{xxy} + \chi_{xyx})cos\theta sin\theta + \chi_{xyy}sin^2\theta \\ \chi_{yxx}cos^2\theta + (\chi_{yxy} + \chi_{yyx})cos\theta sin\theta + \chi_{yyy}sin^2\theta \end{pmatrix} \end{aligned} \tag{A.2}$$

Which, by performing a new rotation at the half-wave plate we obtain $P'_{2\omega}(\theta') = T(-\theta)P_{2\omega}(\theta)$, and by applying Kleimann's symmetry conditions $\chi^{(2)}_{xxy} = \chi^{(2)}_{xyx} = \chi^{(2)}_{yxx}$ and $\chi^{(2)}_{xyy} = \chi^{(2)}_{yxy} = \chi^{(2)}_{yyx}$ we obtain:

$$P'_{2\omega}(\theta') = \begin{pmatrix} \chi_{xxx}cos^3(\theta) + 3\chi_{xyy}cos^2\theta sin\theta + 3\chi_{xyy}cos\theta sin^2\theta + \chi_{yyy}sin^3\theta \\ \chi_{yxx}cos^3(\theta) + (2\chi_{yxy} - \chi_{xxx})cos^2\theta sin\theta + (\chi_{yyy} - 2\chi_{xxy})cos\theta sin^2\theta + \chi_{yxx}sin^3\theta \end{pmatrix} \tag{A.3}$$

Which will in turn give us the parallel intensity by $I_{||}(\theta) = |P'^x_{2\omega}(\theta')|$.

DEPARTMENT OF PHYSICS
CHALMERS UNIVERSITY OF TECHNOLOGY
Gothenburg, Sweden
www.chalmers.se

AVANCEZ
1829
CHALMERS
UNIVERSITY OF TECHNOLOGY